

# **Leveraging data-driven weather models for improving numerical weather prediction skill through large-scale spectral nudging**

Syed Zahid Husain<sup>a</sup>, Leo Separovic<sup>a</sup>, Jean-François Caron<sup>b</sup>, Rabah Aider<sup>a</sup>, Mark Buehner<sup>b</sup>, Stéphane Chamberland<sup>a</sup>, Ervig Lapalme<sup>b</sup>, Ron McTaggart-Cowan<sup>a</sup>, Christopher Subich<sup>a</sup>, Paul Vaillancourt<sup>a</sup>, Jing Yang<sup>a</sup>, and Ayrton Zadra<sup>a</sup>

<sup>a</sup>*Atmospheric Numerical Prediction Research Section, Environment and Climate Change Canada, Dorval, Quebec, Canada H9P 1J3*

<sup>b</sup>*Data Assimilation and Satellite Meteorology Research Section, Environment and Climate Change Canada, Dorval, Quebec, Canada H9P 1J3*

*Corresponding author:* Syed Zahid Husain, syed.husain@ec.gc.ca

ABSTRACT: Operational meteorological forecasting has long relied on physics-based numerical weather prediction (NWP) models. Recently, this landscape has been disrupted by the advent of data-driven artificial intelligence (AI)-based weather models, which offer tremendous computational performance and competitive forecasting skill. However, data-driven models for medium-range forecasting generally suffer from major limitations, including low effective resolution and a narrow range of predicted variables. This study illustrates the relative strengths and weaknesses of these competing paradigms using the GEM (Global Environmental Multiscale) and GraphCast models to represent physics-based and AI-based approaches, respectively. By analyzing global predictions from these two models against observations and analyses in both physical and spectral spaces, this study demonstrates that GraphCast-predicted large scales outperform GEM, particularly for longer lead times. Building on this insight, a hybrid NWP-AI system is proposed, wherein GEM-predicted large-scale state variables are spectrally nudged toward GraphCast predictions, while allowing GEM to freely generate fine-scale details critical for weather extremes. Results indicate that this hybrid approach is capable of leveraging the strengths of GraphCast to enhance the prediction skill of the GEM model. Importantly, trajectories of tropical cyclones are predicted with enhanced accuracy without significant changes in intensity. Furthermore, this new hybrid system ensures that meteorologists have access to a complete set of forecast variables, including those relevant for high-impact weather events.

## 1. Introduction

State-of-the-art numerical weather prediction (NWP) models generally include some form of a dynamical core that solves the nonlinear partial differential equations governing the resolved-scale dynamical and thermodynamical processes within the atmosphere. Solutions from the dynamical core are subsequently combined with tendencies from parameterized physics schemes, representing the unresolved and subgrid-scale processes that are not explicitly accounted for by the dynamical equations. Although statistical approaches have been explored in the past — particularly for downscaling purposes (Yu et al. 2006; Busuioc et al. 2008; Cheng et al. 2014) — physics-based NWP models have long been the foundational approach for operational meteorological forecasting. The recent emergence of data-driven models inspired by artificial intelligence (AI) has, however, started to seriously challenge this well established paradigm.

Keisler (2022) presented an important breakthrough demonstrating considerable potential for weather forecasting with data-driven models. This was quickly followed by Pangu-Weather from Huawei (Bi et al. 2022, 2023), GraphCast from Google-DeepMind (Lam et al. 2022, 2023) and several other models (e.g., Pathak et al. 2022; Chen et al. 2023a,b). In general, these models rely on some form of deep neural network architecture. Like any other application of AI, data-driven weather models necessitate a substantial volume of high quality training data. As a result, all currently available AI-based deterministic global weather simulators are trained on the ERA5 reanalyses (Hersbach et al. 2020) from the European Centre for Medium-Range Weather Forecasts (ECMWF), which is undoubtedly the most comprehensive resource available. The neural network weights within these models are specifically trained to make predictions that closely emulate ERA5.

One important aspect of these AI-based weather emulators that set them apart from the classical NWP models is their computational performance. They can speed up the production of multi-day forecasts by orders of magnitude while using a fraction of the computational resources. Furthermore, many of these models are not only comparable to the NWP models with respect to their prediction accuracy, in terms of a number of the performance metrics, they can even surpass the skill of the IFS (Integrated Forecasting System; Lang et al. 2023) from ECMWF, which is widely accepted as the benchmark within the NWP community (Bi et al. 2023; Lam et al. 2023; Chen et al. 2023a).

Despite their advantages, AI-based weather emulators also have limitations. A major weakness of most of the currently available data-driven models is considerable fine-scale smoothing (Bi et al. 2022; Lam et al. 2022). Notably, data-driven models based on generative AI, e.g., diffusion-based GenCast model from Google-DeepMind (Price et al. 2024), can address the fine-scale smoothing problem to some extent. However, as of now, such approaches generally require considerable increase in computational cost, thereby diminishing one of the principal advantages of the AI models.

Improving the nominal horizontal resolution of the AI model inferences (i.e., forecasts) is also challenging. The general construction of these models requires higher-resolution training data to enable these models to make inferences at higher resolutions. Since the ERA5 reanalysis is only available at  $0.25^{\circ}$  resolution, this restriction means that current global AI models cannot be trained for kilometer-scale forecasting. Another common limitation of the current generation of AI models is the limited range of predicted variables. At present, these models can only be trained to emulate fields that are present in the analyses dataset, although training to predict non-analyzed variables (e.g., precipitation in ERA5) would generally lead to suboptimal inference. Furthermore, adding the full suite of physics-related prognostic variables required for operational NWP, such as categorization of cloud and precipitation types, would be cost-prohibitive with current AI model architectures. Time resolution of inferences is another constraint for most of the current AI models, which make predictions at 6-hour intervals, far coarser than physics-based NWP models. Pangu-Weather (Bi et al. 2022) provides separate models for 1-, 3-, 6-, and 24-hour predictions, but the models with shorter lead times suffer from larger error accumulation. In summary, despite their strengths, the aforementioned limitations make it implausible for the AI models to replace the classical NWP approach in operational weather forecasting.

The GEM (Global Environmental Multiscale) model (Girard et al. 2014), which is employed by Environment and Climate Change Canada (ECCC) for operational weather forecasting, relies entirely on the physics-based NWP approach. The principal objective of this study is to determine whether inferences from a state-of-the-art AI-based weather emulator can be leveraged through large-scale spectral nudging to enhance the predictability of the GEM model, particularly for global weather forecasting. Spectral nudging can be seen as an indirect suboptimal data assimilation method (von Storch et al. 2000). Although the concept of spectral nudging was first proposed

to control spatial computational modes in a limited-area model (LAM; Waldron et al. 1996), it is primarily used to improve dynamical downscaling of coarse-resolution atmospheric model simulations over high-resolution limited area domains (Leduc and Laprise 2009; Husain et al. 2014). Spectral nudging has also been applied for global atmospheric hindcasting (Schubert-Frisius et al. 2017).

The ultimate goal of this study is to develop a hybrid NWP-AI system that combines the strengths of both approaches while addressing the inherent limitations of the AI-based models. The AI model chosen for this study is the GraphCast model from Google-DeepMind. Based on internal testing at ECCC, among the different freely available open-source AI-based models, GraphCast demonstrates the best accuracy with respect to most of the metrics.

To achieve the most optimal fusion of GraphCast and GEM, it is essential to ascertain the relative strengths and limitations of these models through objective evaluation against observations and analyses. A detailed comparative analysis of these models is also critical for devising the most optimal spectral nudging configuration, and therefore, constitutes a significant component of this study.

Spectral nudging has so far been unfeasible for real-time forecasting applications due to the lack of availability of timely and accurate reference data. The emergence of AI models like GraphCast has unlocked the potential for applying spectral nudging in real-time operational weather forecasting. In this regard, application of spectral nudging for enhancing real-time NWP represents an important novelty proposed by this study. Although this paper illustrates the hybridization concept with a specific combination of the AI and NWP models, the proposed strategy is expected to be broadly applicable to any other combination as long as the AI model offers some added value over the NWP model.

This article is organized as follows. Sections 2 and 3 provide some important background information regarding the GEM and GraphCast models, respectively. Details pertaining to the relative performances of these models are documented in section 4. Section 5 covers the concept of spectral nudging, its implementation in GEM as well as the optimal nudging configuration used in this study. Detailed evaluations of the spectral nudging-based hybrid NWP-AI system are presented in 6. Finally, section 7 summarizes the conclusions of this study and outlines potential directions for future work.

## 2. The NWP System

### a. The GEM Model

The dynamical core of the GEM model solves the elastic Euler system of equations. These equations are first transformed from regular height coordinate to some form of a terrain-following coordinate (TFC) in the vertical, denoted by  $\zeta$  in the model. All current operational GEM-based NWP systems employ a log-hydrostatic-pressure-type TFC (Girard et al. 2014; Husain et al. 2021).

The nonhydrostatic version of the dynamical core involves eight prognostic variables: horizontal velocity components ( $u$  and  $v$ ), vertical velocity ( $w$ ), virtual temperature ( $T_v$ ), geopotential ( $\phi$ ), vertical motion with respect to the TFC ( $\dot{\zeta}$ ), hydrostatic surface pressure ( $\pi_s$ ), and nonhydrostatic pressure perturbation ( $q = \ln \frac{p}{\pi}$ , where  $p$  and  $\pi$  denote the complete and hydrostatic pressure, respectively).

The advection terms in the model are treated with semi-Lagrangian approach while a two-time-level iterative implicit Crank-Nicolson type scheme is employed for temporal discretization. Spatial discretization relies on staggered grids: an Arakawa C grid in the horizontal and a Charney-Phillips grid in the vertical. Further details in this regard can be found in the existing literature (Girard et al. 2014; Husain and Girard 2017). Global simulations in GEM utilize a Yin-Yang grid system, where two orthogonal and overlapping LAM grids are combined to construct the global grid (Qaddouri and Lee 2011).

Solutions from the GEM dynamical core are combined with tendencies from parameterized physics schemes that represent unresolved (or partially resolved) physical processes, such as radiation, convection, boundary layer turbulence, surface-atmosphere interactions, condensation, etc. The parameterization schemes are executed in a sequential manner. All operational GEM-based NWP systems rely on a splitting-type mechanism for coupling the parameterized physics tendencies with the resolved dynamics. In this approach, physics-induced tendencies are applied as grid-point adjustments to the dynamics solution to obtain the complete solution for a model time step (Husain et al. 2019).

### b. Global Deterministic Prediction System (GDPS)

The version of the GDPS used in this study is based on its current operational configuration. It has a horizontal grid spacing of approximately 15 km. In the vertical, GDPS employs 84 prog-

nostic vertical levels with the topmost level at approximately 0.1 hPa. The first momentum and thermodynamical levels are approximately 20 m and 10 m away from the surface, respectively. It uses a time-step length of 450 s.

In terms of the underlying physics parameterizations, GDPS has undergone a major modernization in the recent past (McTaggart-Cowan et al. 2019). This includes updated versions of schemes for radiative transfer, blocking, orography gravity waves and non-orographic gravity waves.

Although operational GDPS is coupled with the NEMO ocean model (Smith et al. 2018), all the experiments for this study were conducted with atmosphere-only configurations. As the impact of coupling is usually modest for 10-day forecasts (McTaggart-Cowan et al. 2019), conclusions drawn from this study are expected to generally hold in the presence of atmosphere-ocean coupling.

### 3. The AI-based Prediction System

#### a. *The GraphCast Model*

The GraphCast (GC) model from Google-DeepMind is an AI-based weather emulator which has been trained to emulate ECMWF’s ERA5 reanalyses. It requires the state of the atmosphere at times  $t$  and  $t - \Delta t_{GC}$  to produce a forecast valid at  $t + \Delta t_{GC}$ , where  $\Delta t_{GC} = 6$  hr. Although the model can be employed auto-regressively  $N$  times to generate predictions valid at  $t + N\Delta t_{GC}$ , it is trained to minimize error for up to 12 recursive forecast steps (from 6 hr to 3 days) by considering ERA5 as the ground truth. The objective of such a training is to produce forecasts with reasonable skill for up to day 10.

At its core, GC employs graph neural networks (GNNs) with an “encoder-processor-decoder” configuration (Lam et al. 2022, 2023). The input and output states of GC are represented over a  $0.25^\circ$  latitude-longitude global grid. A major advantage of GNNs is the possibility of having arbitrary range of spatial interactions. GraphCast takes advantage of this GNN feature by introducing a multi-mesh architecture based on iteratively-refined icosahedral grids (from level-0 to level-6 refinements) within the processor component. The encoder of GC maps data from the input  $0.25^\circ$  latitude-longitude grid to the internal multi-mesh of the processor, whereas the decoder brings back information from the processor multi-mesh to the output grid.

The internal multi-mesh of GC processor is spatially homogeneous. The highest resolution (level-6) mesh has a nominal resolution of  $1^{\circ}$  with 40,962 nodes, while the nodes of the coarse-resolution meshes are subsets of these nodes. This facilitates multi-scale graph edges that connect the highest-resolution mesh nodes to the nodes associated with the coarse-resolution meshes to achieve multi-mesh message passing. Such an approach, therefore, leads to multi-scale interactions ranging from synoptic to mesoscales.

The atmospheric state predicted by GC is represented by 6 variables defined on multiple pressure levels (temperature,  $u - v$  components of wind, geopotential, specific humidity, and vertical wind speed) and 5 surface variables (2-m temperature, 10-m wind components, mean sea-level pressure, and total precipitation). In addition to the predicted variables, the input system of GC requires time-dependent forcing in the form of total incident solar radiation at the top of the atmosphere along with information regarding the local time of the day and progression of year. These time-dependent forcing terms are computed analytically. Furthermore, the input system requires some stationary input features like the land-sea mask, surface geopotential as well as information on the local longitude and latitude of its input grid.

Pre-trained weights of GC (learned features of the GNNs) are available from Google-DeepMind for two different sets of pressure levels. The version with higher vertical resolution has 37 pressure levels with the top at 1 hPa, while the coarser-resolution version has only 13 levels with the top at 50 hPa (Lam et al. 2022). It is important to note that, in addition to training on ERA5, the 13-level GC was also fine-tuned by DeepMind on initial conditions for ECMWF's operational IFS system, from 2016 to 2021.

### *b. GraphCast-based Global Prediction System*

An experimental GC-based global prediction system has been developed at ECCC. Both the 37-level and 13-level versions of GC are available. This system takes the GDPS operational analyses (Caron and Buehner 2022) as its input. However, the GNN weights have not been subjected to any fine-tuning at ECCC. All GC predictions utilized in this study are based on this experimental system.

Based on the evaluation of GC predictions with the GDPS analyses as input, the 13-level version of GC (GC-13L) outperforms the 37-level version (GC-37L) for most variables, at most levels and

over most regions of the world. This is presumably due to the fact that stratospheric specific humidity in the GDPS analyses generally differs from ERA5 by an order of magnitude creating large imbalances when 37-level GC (with multiple levels in the stratosphere) is initialized with the GDPS analyses. The previously mentioned additional fine-tuning of GC-13L by DeepMind could also have contributed to its superior performance. This study is, therefore, entirely based on the GC-13L and, henceforth, GC is used to refer to GC-13L.

## 4. Relative performances of the GDPS and GC forecasts

### *a. Experimental setup*

Ten-day forecasts from GC and GDPS are initialized using the GDPS analysis every 36 h, leading to 60 cases for boreal winter 2022 (from 01 December 2021 at 0000 UTC to 27 February 2022 at 1200 UTC) and 62 cases for boreal summer 2022 (from 01 June 2022 at 0000 UTC to 31 August 2022 at 1200 UTC). This version of GDPS, which includes data assimilation and forecasting components, became operational in June 2024 (ECCC 2024). Henceforth, the GDPS experiment based on this configuration will be referred to as GDPS-CTL.

### *b. Verification with global power spectra*

Although GC employs a  $0.25^\circ$  latitude-longitude resolution grid, its predictions are subject to a smoothing effect, which increases with lead time. This is generally assumed to be associated with learning to minimize the mean square error (MSE) (e.g., Keisler (2022), Lam et al. (2023)). The smoothing effect is well indicated by departures of 120-h GC forecasts' global 250-hPa kinetic energy and 500-hPa temperature variance spectra from those of GDPS-CTL forecasts and the analyses (Fig. 1). GraphCast's spectra are steeper, leading to a notable variance deficiency at wavenumbers as low as 30, corresponding to lower synoptic and sub-synoptic scales ( $< 1500$  km). However, both GDPS-CTL forecasts and analyses much more closely follow the  $k^{-3}$ -law, pertaining to the 3-dimensional quasi-geostrophic flow (Charney 1971; Skamarock et al. 2014), which indicates that GC slopes are not realistic. Hence, the effective resolution of GC, defined as the highest wave number at which the atmospheric variability is still adequately represented, is considerably lower than its nominal resolution. Conversely, the effective resolution of the classical NWP models is typically about 6~8 times their nominal resolution, i.e., grid spacing (Ska-

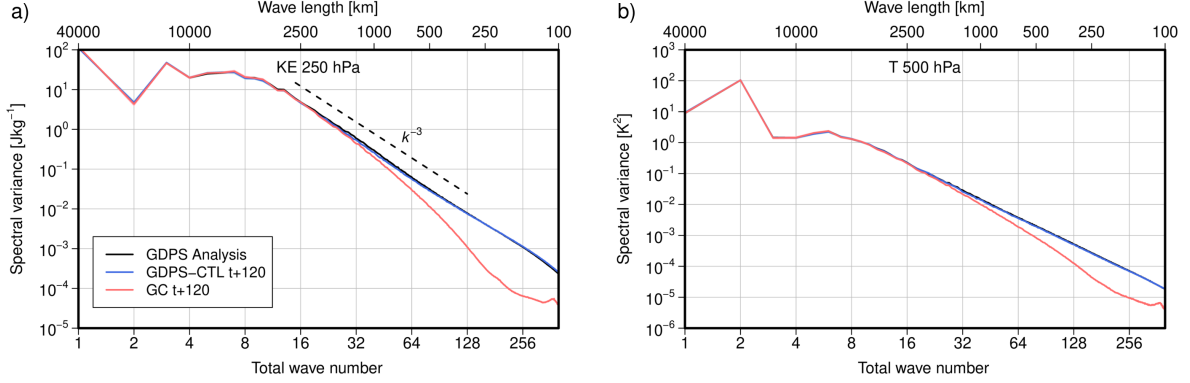


FIG. 1. Global (a) kinetic energy power spectrum of 250-hPa horizontal wind and (b) variance spectrum of 500-hPa temperature after 120 h of integration for the GDPS analyses (black), GDPS-CTL (red) and GC (red), averaged over 60 cases of boreal winter 2022. The dashed line indicates the  $-3$  slope.

marock 2004). With the current operational configuration, the nominal resolution for GDPS-CTL is  $0.1375^\circ$ , leading to an effective resolution of around 90-100 km.

It is important to note that the stationary effects of orography, land-sea contrast and large latitudinal climatological variations tend to be much less affected by smoothing in GC than the less predictable transient anomalies. It is therefore useful to introduce the transient spectral amplitude ratio, defined as follows:

$$\gamma = \left( \frac{\overline{\sigma_{x'x'}}}{\overline{\sigma_{y'y'}}} \right)^{1/2}, \quad (1)$$

where  $\sigma_{x'x'}$  and  $\sigma_{y'y'}$  are the power spectra of the forecast' and analysis' transient-eddy components, respectively, and the overbar denotes averaging over the cases for a given season. The forecast transient eddies are defined as  $x' = x - \bar{x}$ , and similarly for the analysis. Figure 2 shows the evolution of  $\gamma$  with lead time for GC and GDPS-CTL forecasts, against the GDPS analysis. While  $\gamma$  remains close to 1 for all lead times for GDPS-CTL, indicating that its effective resolution does not change during the integration, for GC it rapidly decreases, leading to an effective resolution as low as 1000 km for 24-h forecasts. The smoothing effect further reduces the effective resolution to 2500~2700 km before it saturates around forecast days 3–5. It is worth noting here that GC still resolves scales smaller than these limits, but only partly ( $0 < \gamma < 1$ ). While designing any strategy to leverage GC predictions to improve GEM, it would be prudent to not

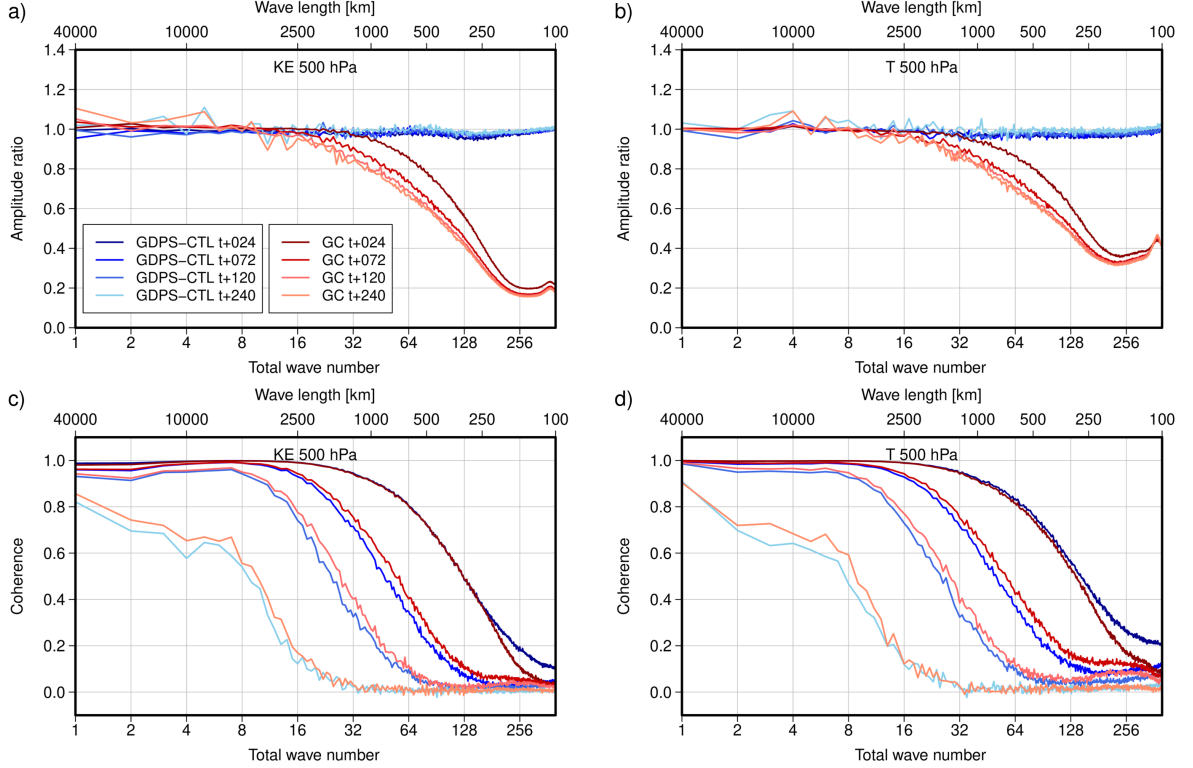


FIG. 2. Spectral (a, b) amplitude ratio  $\gamma$  and (c, d) coherence  $\rho$  for the global (a, c) kinetic energy spectrum of 500-hPa horizontal wind transient-eddy deviations and (b, d) variance spectrum of 500-hPa temperature transient-eddy deviations, or GDPS-CTL (blue) and for GC (red), after (dark to light) 24, 72, 120 and 240 h of integration. Spectra are averaged over 60 cases of boreal winter 2022.

force the GEM model to follow GC for these variance-deficient scales in order to not adversely affect GEM's effective resolution. This will be revisited in Section 5, where the concept of spectral nudging and its implementation in GEM are discussed.

Figure 2 also displays the spectral coherence defined as follows:

$$\rho = \frac{\overline{\sigma_{x'y'}}}{(\overline{\sigma_{x'x'}} \overline{\sigma_{y'y'}})^{1/2}} , \quad (2)$$

where  $\sigma_{x'y'}$  is the transient-eddy co-spectrum between the GDPS-CTL or GC forecasts and the GDPS analyses. Since the same GEM model is used to produce both the GDPS forecasts and backgrounds for the analysis steps, they may have common systematic errors, especially at shorter lead times. This may unfairly penalize GC, which is trained on ECMWF-ERA5 reanalyses. De-

spite that, Fig. 2 clearly indicates an improved spectral coherence with the GDPS analyses for a large range of scales – from synoptic to planetary, especially at longer lead times. This suggests that forcing GEM toward GC has potential for improving the predictive skill of its transient-eddy anomalies.

### *c. Verification against radiosondes*

At ECCC, model developers often rely on forecast verification against ECMWF-HRES analysis (Lang et al. 2023) to avoid the problem associated with own-analysis verification (see, e.g., Casati et al. (2008), Privé et al. (2021)). This also helps to get around the issue of inhomogeneity of the observing network. Since GC was primarily trained with the ERA5 reanalysis and then fine-tuned on the ECMWF-HRES analysis, this likely introduces some dependency on the ECMWF analysis systems. To ensure that the dataset used to verify the forecasts is completely independent from both models as well as the GDPS data assimilation system, it was opted to rely mainly on observations from the global radiosondes network. Observations of zonal wind ( $U$ ), geopotential height ( $Z$ ), temperature ( $T$ ) and dewpoint depression ( $T - T_d$ ) at mandatory pressure levels between 1000 and 100 hPa will therefore be used as reference for verification.

Two flavors of the verification against radiosonde observations are performed: (1) verification at full resolution, with the GDPS-CTL and GC forecasts at their native resolution, and (2) verification at low resolution — corresponding to the effective resolution of GC – wherein both the GDPS-CTL and GC forecasts are filtered to remove the variability at scales not adequately resolved by GC. The fact that GC has a much lower effective resolution than GDPS-CTL would otherwise provide an unfair advantage to GC by reducing the so-called “double penalty” for misplacing the predicted patterns. Low-resolution verification against radiosondes also allows the study of how suitable GC forecasts are for large-scale spectral nudging in GEM.

The filter applied here is a spectral filter based on spherical harmonics. It approximately removes scales smaller than 1000 km (total wavenumber 40) and fully preserves scales larger than 2000 km (wavenumber 20). These cutoff wavenumbers well reflect the effective resolution of GC at forecast days 3 to 5 (See Figs. 2a and b). Note also that the same filter configuration is applied to GC and GDPS-CTL (more details on this filter can be found in Appendix A).

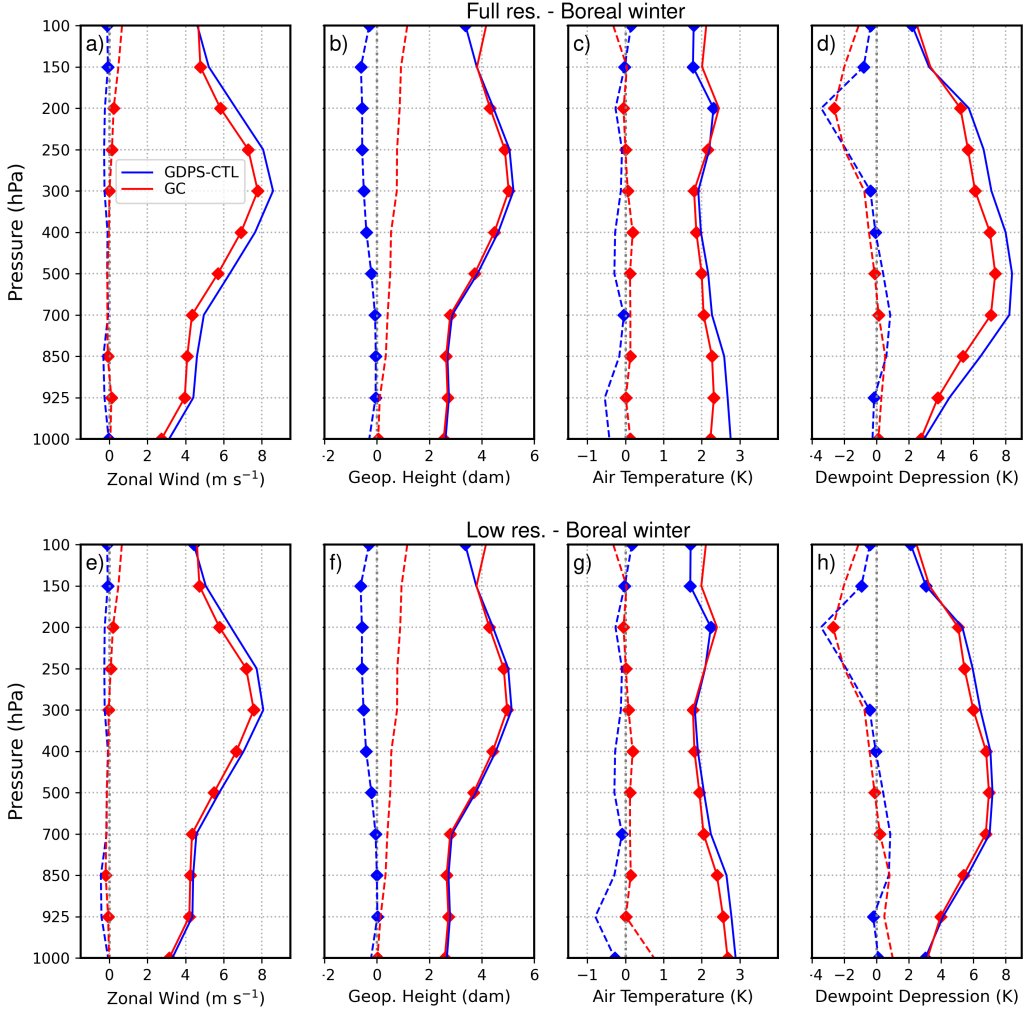


FIG. 3. Verification for 120-h forecasts from GC (red) and GDPS-CTL (blue) at their full (top row: a–e) and low (bottom row: e–h) resolutions against global radiosonde observations, averaged over 60 cases in boreal winter. The error standard deviation (STDE; solid lines) and bias (mean forecast minus observation; dashed lines) are shown for (a,e) zonal wind, (b,f) geopotential heights, (c,g) temperature and (d,h) dewpoint depression. Red and blue markers denote statistically significant differences in favor of GC and GDPS-CTL, respectively. Significance is computed using the *t*-test for bias and the *F*-test for STDE. No marker at a pressure level implies that the null hypothesis, stating that the statistics of the two samples are the same, cannot be rejected based on the 90th percentile. A low pass filter (Appendix A) is applied on both GC and GDPS-CTL to obtain the low-resolution fields (e–h).

## 1) AT FULL RESOLUTION

Comparing the forecasts at their native resolution to the radiosonde observations reveals that for most variables and lead times, and for levels between 1000 and 200 hPa, GC forecasts are much closer to the observations than GDPS-CTL. Vertical profiles of error averages (bias) oriented as forecast minus observation and error standard deviations (STDE), calculated over the global domain for 120-h forecasts for boreal winter, highlight the typical verification differences between GC and GDPS-CTL (Fig. 3a–d). The differences between GC and GDPS-CTL in terms of biases are mixed, except for temperature during boreal winter, where clear improvements can be seen with GC. In terms of STDE, however, GC clearly shows large improvements over GDPS-CTL at almost every level, and particularly for zonal wind and dewpoint depression. Above 200 hPa, however, GC suffers from increased errors, with biases and STDE being comparable or worse than those in GDPS-CTL.

To summarize the scores at different lead times, variables and vertical levels a single forecast quality index based on the fractional root-mean-square error (RMSE) change is defined as follows:

$$f_{RMSE} = \left[ \frac{RMSE(x_1)}{RMSE(x_2)} - 1 \right] \times 100\%, \quad (3)$$

with  $x_1$  and  $x_2$  here representing GDPS-CTL and GC, respectively. Positive values of  $f_{RMSE}$  thus imply improved forecasts from GC measured by the RMSE against the radiosonde observations, while negative values represent the opposite. The forecast quality index  $f_{RMSE}$  was computed every 24 h for each selected variable and level. The results for each variable were then vertically averaged for three layers: low-level (from 1000 to 850 hPa), mid-level (from 700 to 300 hPa) and high-level layer (from 250 hPa to 100 hPa).

TABLE 1. Latitude and longitude bounds for the 6 subdomains considered in Figures 5, 11 and 13.

Domain	Southern Bound	Northern Bound	Western Bound	Eastern Bound
Northern Hemisphere	20N	90N	-	-
Southern Hemisphere	90S	20S	-	-
Tropics	20S	20N	-	-
North America	25N	85N	170W	40W
Europe	25N	70N	10W	28E
Asia	25N	60N	65E	145E

Results for boreal winter (see Fig. 4a) show that  $f_{RMSE}$  is quite constant with lead times for each variable and layer. The largest improvements from GC are obtained in the low-level layer for all variables and decrease with altitude, turning into deteriorations in the high-level layer for geopotential heights and temperatures. GraphCast geopotential heights are also degraded with respect to GDPS-CTL in the mid-level layer at short lead times. Results for boreal summer are roughly similar (not shown). The pressure weighting approach adopted for the training of GC (see Fig. 6 in Lam et al. (2022)) is likely responsible for this vertical variation in performances. The differences in the upper-level layer between ECMWF-ERA5 and GDPS analyses used for GC initial conditions (e.g., different bias correction approaches for radiances, different data assimilated, distinct biases in the IFS and GEM model, etc.) could also explain some of the degradations observed in the upper-level layer when GC is initialized with the GDPS analysis. However, GC initialized with ECMWF-ERA5 has also been shown to increase the RMSE with respect to ECMWF-HRES above the tropopause when compared to analyses (see, e.g., Fig. 19 in Lam et al. (2022)).

The region-wise variations in relative forecast performances can be examined by computing, as above, the forecast quality index  $f_{RMSE}$  averaged over all variables and lead times for each vertical layer but, this time, for the 6 subdomains listed in Table 1 with their respective latitude and longitude limits. In low- and mid-level layers, GC forecasts show smaller RMSE in every subdomain in both seasons (Figs. 5a and c). In the upper-level layer, GDPS-CTL performs better during each hemisphere's respective winter. However, GC's poor performance during winter over the northern hemisphere is primarily originating from Europe. The largest improvements from GC in the mid- and high-level layers are found over the Tropics, which is consistent with the results of Lam et al. (2022) (see their Fig. 19).

## 2) AT LOW RESOLUTION

At low resolution, the forecast improvements in terms of RMSE from GC over GDPS-CTL are significantly reduced for all variables, levels, lead times, seasons and geographical domains (Figs. 3e–h and 4). This reduction in improvements at low resolution is particularly striking in the mid-level layer over the first 72 h (compare Figs 4a and b), leading to growing forecast improvements with time from GC that saturate or peak near 120 h (Fig. 5b) compared to a relatively steady improvement at all lead times found with the full resolution (Fig. 4a). This suggests that the

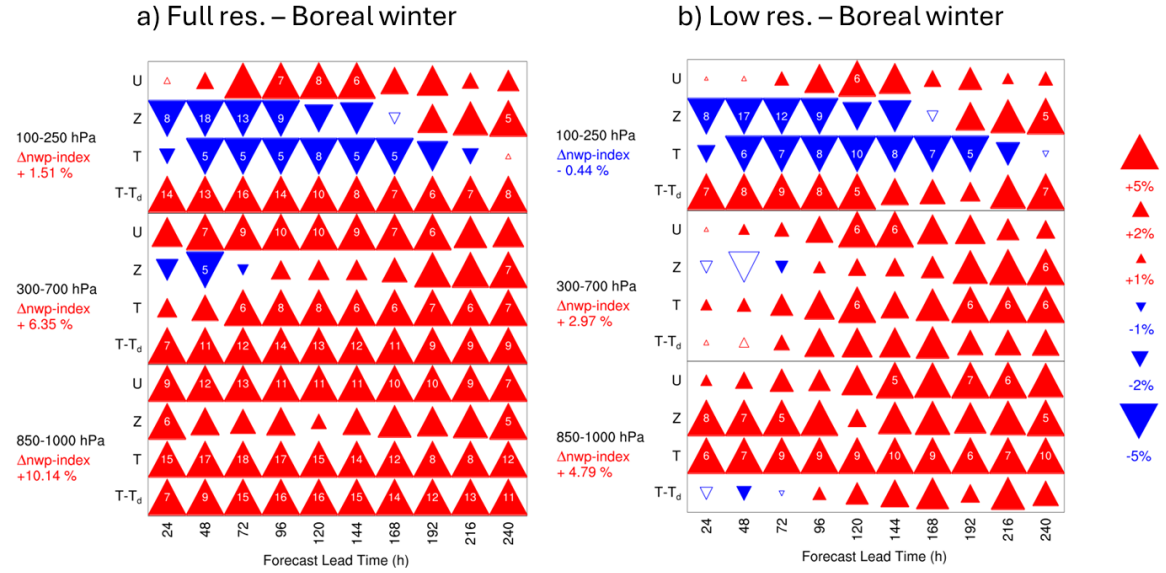


FIG. 4. Changes in the forecast quality index (Eq. 3) against global radiosonde observations, averaged over 3 layers and 60 cases during boreal winter 2022, corresponding to forecasts at (a) high resolution and (b) low resolution. Upward-pointing red triangles indicate a reduction of the RMSE in GC forecasts with respect to GDPS-CTL, whereas downward-pointing blue triangles indicate the opposite. The size of the triangles varies linearly up to a value of 5.0%. When the index is greater than this threshold, the size is kept constant, but the rounded values are shown. Triangles are color-filled if the significances computed using an *F*-test exceeds the 90th percentile. The values on the left-hand side show the averaged indices over all the lead times and all the variables for each layer.

improvements with GC for the first 72 h at full resolution largely originate from partial smoothing of the less-accurately predicted fine scales that reduces the double penalty.

Degradations in GC, seen at full resolution over Northern Hemisphere in boreal winter (mostly coming from Europe) and Southern hemisphere in boreal summer, are enhanced at low resolution (compare Figs 5a, c, and 5b, d). There are also notable degradations in the mid- and low-level layers over Asia in summer (Fig. 6d). The average reduction factor for  $f_{RMSE}$  from full- to low-resolution verification is roughly between 2 to 3 (compare the left and right columns in Fig. 5), which confirms that the lower effective resolution of GC provides a significant advantage over the GDPS-CTL. Nevertheless, large scales of GC forecasts are still, on average, significantly closer

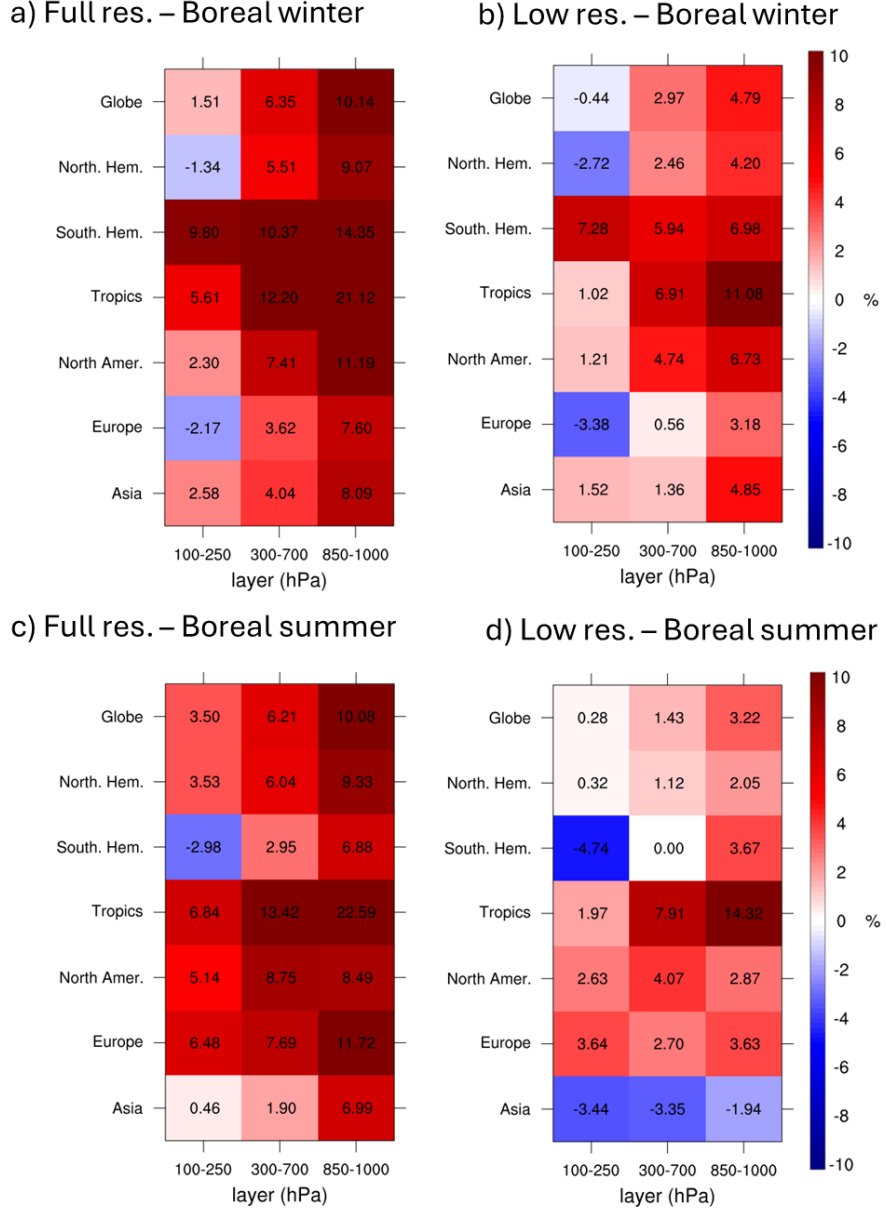


FIG. 5. Heatmap of the changes in the forecast quality index (Eq. 3) against global radiosonde observations for various geographical domains and atmospheric layers for (a, b) 60 cases of boreal winter 2022 and (c, d) 62 cases of boreal summer 2022. Verifications are presented for forecasts (a, c) at their full resolution and (b, d) after applying a low pass filter (Appendix A) on both GC and GDPS-CTL. Red shadings indicate a reduction of the RMSE by GC with respect to GDPS-CTL, while blue shadings indicate the opposite.

to the radiosonde observations than those from GDPS-CTL in the mid- and low-level layers. This suggests that nudging these large-scale components of key GEM state variables toward GC could result in substantial improvements over GDPS-CTL.

## 5. Spectral nudging in GEM

### *a. The concept*

Spectral nudging operates by gradually directing the model-predicted atmospheric large scales towards those found in some reference data which is considered to have a more accurate representation of those scales. This approach fundamentally differs from grid nudging or indiscriminate nudging, as it only targets a predefined range of scales. Even though an NWP model may employ grid-based spatial discretizations, the nudging increments at a given model level are computed by decomposing the model predictions and the reference fields in a spectral space, retaining only the target scales. Hence, this technique is referred to as “spectral nudging”.

In limited-area configuration, such as regional climate models, the nudging reference is usually derived from the same data that provides the lateral boundary conditions (LBCs). For extended-range integrations – spanning weeks to months or even years – the LBCs alone are insufficient to prevent the model-predicted large scales from drifting significantly. Consequently, spectral nudging becomes essential (Leduc and Laprise 2009). For multi-month kilometer-scale downscaling applications, the evolving surface fields may also exhibit unacceptable deviations, necessitating nudging toward a reliable reference, as discussed by Husain et al. (2014).

### *b. Implementation in GEM*

With the split-adjustment-type dynamics-physics coupling in GEM, the adiabatic dynamical core first solves the prognostic dynamical equations to obtain an intermediate state of the atmosphere. In the absence of spectral nudging, this interim dynamics solution serves as the input for the physical parameterization schemes, which compute the physics-induced tendencies. These tendencies are then coupled with the dynamics solution to obtain the complete model solution for a given time step. However, when spectral nudging is applied, the large scales in the solutions for a selected set of prognostic variables from GEM dynamics are first nudged toward the reference (here, from GC). Subsequently, the nudged solutions are fed to the physics schemes to compute the

physics-induced tendencies before the eventual dynamics-physics coupling, following the regular model procedure.

In mathematical form, the nudging step at a given model vertical level, i.e., a constant- $\zeta$  surface, can be expressed as

$$F_{nudge} = F_{GEM} + \omega [F_{GC} - F_{GEM}]_{LS}, \quad (4)$$

where  $F_{GEM}$  is a prognostic variable predicted by GEM dynamics,  $F_{GC}$  is the corresponding prediction from GC valid at the same time,  $\omega$  is the nudging relaxation factor such that ( $0 \leq \omega \leq 1$ ), and  $F_{nudge}$  is the nudged solution. The subscript  $LS$  in the above equation refers to some user-defined large scales targeted by the nudging mechanism. Through simple rearrangement of the terms on the right-hand-side of Eq.4, it can be shown that the large scales in  $F_{nudge}$  are indeed a weighted average of those from  $F_{GEM}$  and  $F_{GC}$  (with  $\omega$  being the weighting parameter), whereas the small scales from  $F_{GEM}$  are retained entirely in  $F_{nudge}$ .

As shown by Husain et al. (2014),  $\omega$  can vary with model vertical levels and in time, and is given by

$$\omega = \frac{\beta(\zeta)}{\tau(t)} \Delta t, \quad (5)$$

where  $\beta(\zeta)$  defines the nudging vertical profile with respect the  $\zeta$ -coordinate,  $\tau(t)$  represents the nudging relaxation time scale, and  $\Delta t$  denotes the model time-step length (in the same unit as  $\tau$ ). A vertically-variable  $\beta$  allows for different nudging strengths at different model levels. Conversely, a time-dependent  $\tau$  permits changing nudging strengths with time. In general, a large value of  $\tau$  implies weak nudging, and vice versa.

To nudge a prognostic variable  $F$  at any model level, it is first essential to spectrally decompose  $(F_{GC} - F_{GEM})$  so that a filter can be applied in the spectral space to retain only the desirable scales. Spherical harmonics-based spectral decomposition would be the ideal choice for such a filter. However, this would require multiple transformations of model solutions between the model's Yin-Yang grids and an intermediate global Gaussian grid, resulting in significant increase in the computational cost. As the present study is primarily of a proof-of-concept nature, in order to keep the approach simple, the spectral filter for nudging was instead chosen to be based on

discrete cosine transform (DCT) (Denis et al. 2002), and the filtering is performed separately on the Yin and Yang grids. Additionally, nudging is also separately applied to the Yin and Yang grid solutions after every dynamics sub-step.

Large scales that are retained with spectral nudging are defined by users through configurable parameters. Instead of an abrupt cut-off for the target scales, which may lead to Gibbs phenomena (Sardeshmukh and Hoskins 1984), a soft cut-off is employed within the DCT-based spectral filter. With this method, the spectral filter relies on two different cut-off scale parameters denoted by  $\lambda_{LS}$  and  $\lambda_{SS}$  such that scales larger than  $\lambda_{LS}$  are fully retained while those smaller than  $\lambda_{SS}$  are completely eliminated. A partial filtering, similar to the one utilized by Husain et al. (2014), is applied for the scales in between  $\lambda_{LS}$  and  $\lambda_{SS}$ . Further information on the DCT-based filter and its response is provided in Appendix B.

### *c. Optimal configuration*

A series of systematic sensitivity experiments was carried out to identify an optimal spectral nudging configuration for GDPS. All subsequent results presented in the following section are based on this optimal configuration which, from this point onward, will be referred to as GDPS-SN. It is important to note that spectral nudging is currently only applied within the forecasting component of GDPS, i.e., GDPS-CTL, GDPS-SN and GC are all initialized with the same analyses.

Some key aspects of this optimal setup are discussed below.

#### 1) NUDGED VARIABLES

Nudging is only applied to the  $u$ - $v$  components of wind and virtual temperature. While nudging specific humidity can improve the global bias of temperature and humidity in the boundary layer, the computational cost outweighs the benefits. Moreover, nudging specific humidity tends to negatively impact tropical cyclone intensity during the tested period, making it less desirable.

#### 2) NUDGING VERTICAL PROFILE

Although different vertical profiles, defined by  $\beta(\zeta)$ , have been explored, a plateau-shaped profile, as shown in Fig. 6, is found to yield the best results. This profile involves no nudging in the boundary layer (below 850 hPa) and the stratosphere (above 250 hPa). Relatively weaker

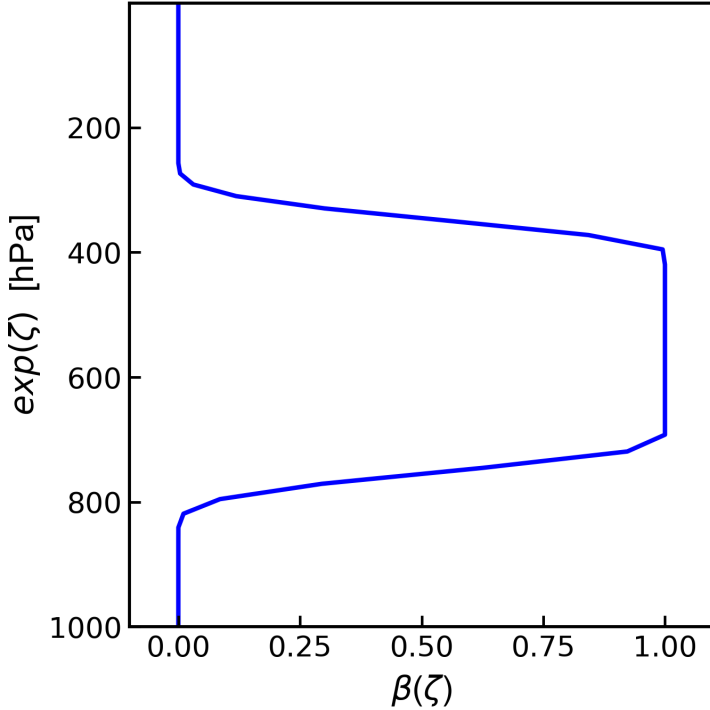


FIG. 6. Nudging vertical profile for the presented optimal configuration, where  $0 \leq \beta(\zeta) \leq 1$  with  $\zeta$  being the log-hydrostatic-pressure-type terrain-following vertical coordinate in GEM. The value of  $\beta$  is set to zero when  $\exp(\zeta) > 700$  hPa and  $\exp(\zeta) < 250$  hPa. Its value is set to 1 for  $400 \text{ hPa} \leq \exp(\zeta) \leq 250 \text{ hPa}$ . Transition of  $\beta$  from 0 to 1 (and vice versa) follows a cosine-squared profile similar to the one presented by Husain et al. (2014).

performance of GC in the stratosphere – as has been mentioned earlier – is the reason for no stratospheric nudging. Within the boundary layer, nudging is avoided to prevent potential negative impacts arising from inconsistencies between the surface forcing in GDPS and GC training data (ERA5). Furthermore, GC-13 does not have sufficient vertical resolution in the boundary layer to provide a useful reference.

### 3) NUDGING LENGTH SCALES

It has been already shown that the fine-scales in GC suffer from considerable smoothing, worsening at longer lead times (see Figs. 1 and 2). The implementation of spectral nudging in GEM allows for time-varying cut-off scales for nudging. However, the improvements with such an ap-

proach over a stationary cut-off scale are found to be negligible. Therefore, based on the comparison of spectra between GDPS and GC, the DCT-based filter for the optimal configuration utilized in this study is configured with  $\lambda_{LS}=2750$  km and  $\lambda_{SS}=2250$  km. This implies that scales larger than 2750 km are entirely retained, while those smaller than 2250 km are completely eliminated. The scales in between are subjected to partial filtering (see Fig. B1). This choice of nudging length scales corresponds to the effective resolution of GC beyond day 3 (see Figs. 1 and 2).

#### 4) NUDGING RELAXATION TIME

The nudging relaxation time,  $\tau$ , is analogous to the  $e$ -folding time as it determines the time-rate of decay in the large-scale differences between the model and the driving data in the absence of any other process. Arguably,  $\tau$  is one of the most important configurable parameters for spectral nudging. However, selecting an optimal  $\tau$  is not straightforward. First, it is important to note that GC inferences are only available every 6 hours and become increasingly inaccurate with longer lead times (as demonstrated by spectral coherence in Fig. 2). During model integration, when a valid GC inference is not available at certain time steps, an estimate is approximated through linear interpolation between two consecutive GC inferences around the time of interest. In this regard, Omrani et al. (2012) have argued that  $\tau$  should not be less than  $\tau_a$  which denotes the time interval between consecutive driving fields (here, GC inferences). Strong nudging with  $\tau < \tau_a$  can lead to erroneous evolution of nudged fields. Furthermore, sensitivity experiments carried out during this study revealed considerable deterioration of model's skill over complex terrain with  $\tau < \tau_a$  (not shown). As a result,  $\tau_a$  may safely be considered the lower bound for  $\tau$ .

It is also crucial to ascertain an acceptable upper bound for  $\tau$ . Intuitively, as the accuracy of reference nudging data worsens with increasing forecast lead time, it might seem prudent to employ a large  $\tau$ . However, sensitivity experiments have revealed that too large of a nudging relaxation time ( $\tau > 24$  hr) can result in excessive undesirable smoothing in the nudged fields around the cut-off scales developing at day 3 or 4. Eventually, this smoothing affects all scales by day 10 of the forecast (not shown). This increased smoothing with overly large  $\tau$ , is caused by the averaging effect resulting from blending two forecasts, with  $\tau = 48h$  maximizing the effect. Based on the insights derived from the sensitivity tests, a nudging relaxation time of 12 hr is chosen to be optimal.

## 6. Impact of large-scale spectral nudging

### a. *Verification with global power spectra*

The power spectra of the GDPS-SN forecast variables remain approximately the same as in the GDPS-CTL (Fig. 7), which essentially demonstrates that the new hybrid system can adequately resolve the full range of scales present in the GDPS-CTL, without significant smoothing. The resulting spectral amplitude ratio of transient-eddy anomalies,  $\gamma$  (Eq. 1), also has values very close to one for all prognostic variables, lead times and spatial scales for both GDPS-CTL and GDPS-SN. This provides a solid proof-of-concept for the spectral nudging approach (Fig. 8). The only exception is a 10-percent reduction of  $\gamma$  for scales between 2000 and 4000 km at lead times approaching day 10 (wavenumbers 10-20 in Figs. 8a, b). This reduction is explained by GC having some variance deficiency at the corresponding range of scales (2000-2750 km) for longer lead times (beyond day 4). Sensitivity tests with time-varying cut-off length scales that more strictly follow GC's time-evolving effective resolution, showed that this issue could be avoided, but at the expense of significantly reduced GDPS-SN forecast improvements with respect to the GDPS-CTL. This is caused by a weaker constraint being imposed on GDPS-SN towards GC at synoptic scales by such a configuration.

Comparison of the spectral coherence (Eq. 2) between the forecasts and GDPS analysis shows an improved skill of GDPS-SN over GDPS-CTL (Figs. 8c, d). These improvements are somewhat weaker than those seen with GC at shorter lead times (up to day 5), but become comparable beyond day 5 (Figs 2c, d). The scales relevant for improvements at shorter lead times are smaller than those included in the spectral nudging configuration. Nudging the smaller scales would therefore bring the coherence on par with GC but it would lead to variance deficiency, as discussed earlier.

An illustrative example of the value added by the new hybrid system over GC is provided in Fig. 9. Large-scale features of transient-eddy anomalies in GDPS-SN tend to be better (but not fully) aligned with GC than with GDPS-CTL, while containing similar level of fine-scale details as in GDPS-CTL. Figure 10 suggests that large-scale components of GDPS-SN forecast fields are preconditioned with the piloting AI model. Therefore, further improvements to its predictions have potential for similarly improving GDPS-SN.

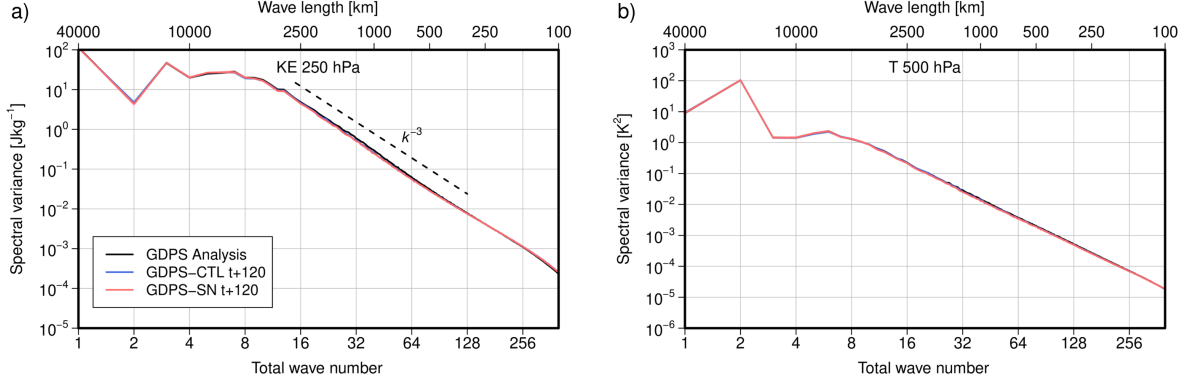


FIG. 7. Same as in Fig. 1, but for the analysis, GDPS-CTL and GDPS-SN.

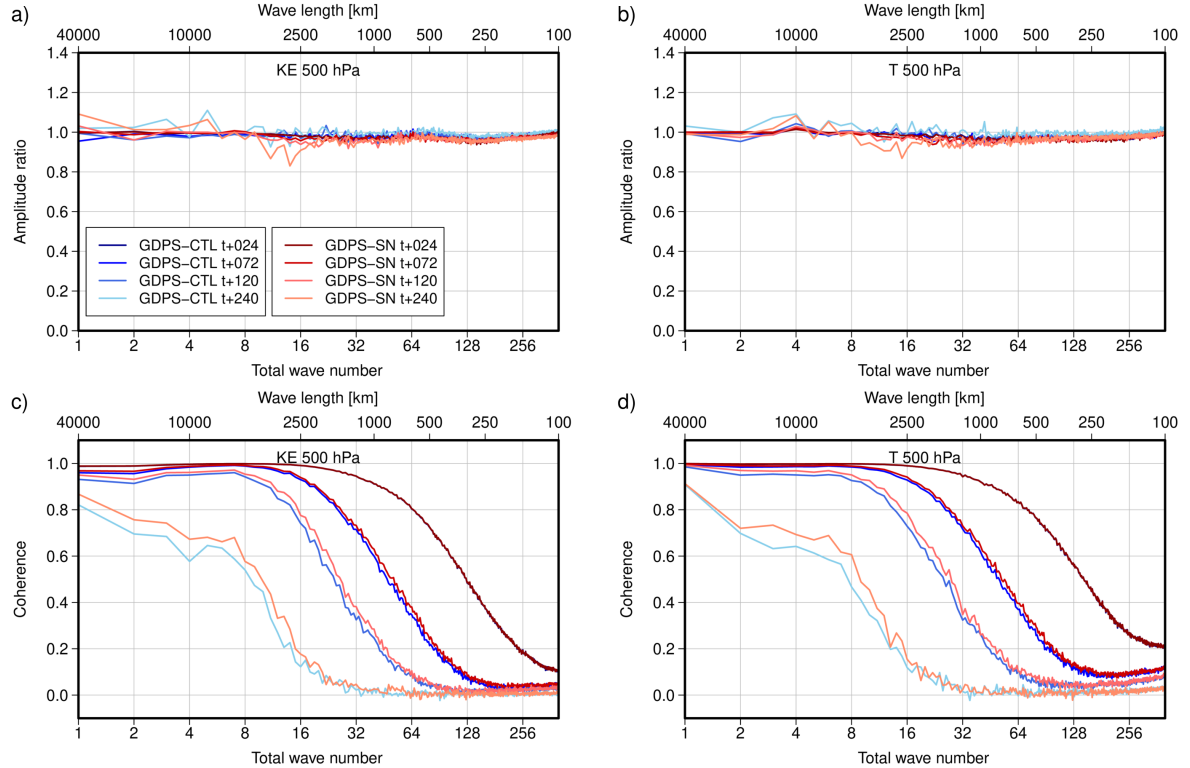


FIG. 8. Same as in Fig. 2, but for GDPS-SN and GDPS-CTL.

### b. Verification against radiosondes

Comparison of forecasts at full resolution against the global radiosonde observations clearly indicates that GDPS-SN forecasts are closer to the observations than GDPS-CTL forecasts for basically all variables, lead times and levels, and over both seasons (Fig. 10). The improvements

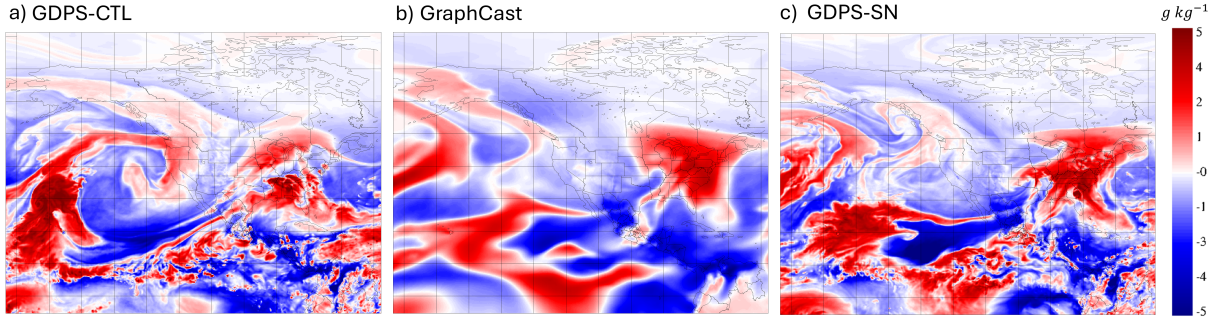


FIG. 9. 10-day forecast of 700-hPa transient-eddy specific humidity anomalies, valid 22 February 2022 at 12z for (a) GDPS-CTL, (b) GC and (c) GDPS-SN.

gradually grow in the first 72 h and are remarkably constant with altitude, which contrasts with the strong vertical variations observed with GC in Section 4. This demonstrates that large-scale spectral nudging, despite being only applied in the mid-level layer for winds and temperature, is sufficient to impart similar improvements at both upper- and lower-level layers that are not constrained by spectral nudging. Compared to boreal winter (Fig. 10a), the improvements from GDPS-SN are reduced by a factor of about 2 during boreal summer (Fig. 10b), which is not surprising given that the benefits from GC over GDPS-CTL at the large scales are smaller by about the same factor for zonal wind and temperature in the mid-level (not shown).

In terms of region-wise performances, the GDPS-SN has smaller RMSE than GDPS-CTL in every subdomain except over Asia in the mid- and upper-levels during boreal summer (Figs. 11c and d), which is relatively consistent with the degradations from GC over the GDPS-CTL at the large scales previously noted for the mid-levels over that part of globe during this season (see Fig. 5d). Unlike GC, the improvements from GDPS-SN over GDPS-CTL are virtually identical when only the large-scale components of the forecast are compared to the radiosonde observations (compare the left and right columns in Fig. 11 and, again, in Fig. 6). This does not necessarily imply that the improvements only originate from the large scales. It rather implies that the relative RMSE reductions with GDPS-SN are of similar level for both the large and small scales. In other words, as the small scales are generally conditioned by the large scales, these results suggest that the fine scales predicted by GDPS-SN benefit from fractional improvements that are on par with its large-scale skill enhancement.

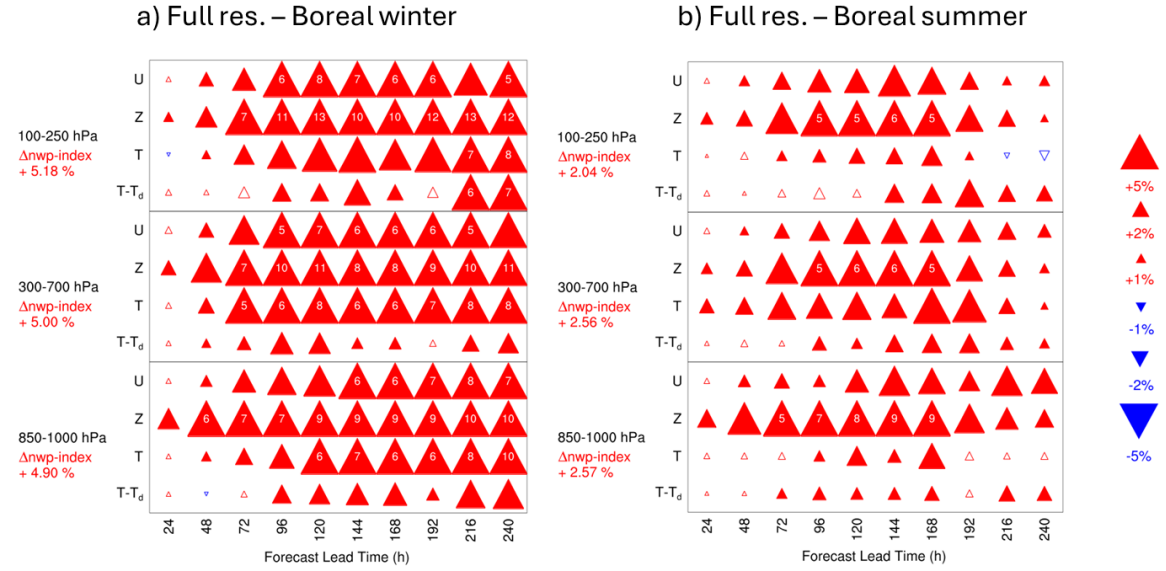


FIG. 10. Same as in Fig. 4, except that upward-pointing red triangles indicate a reduction of the RMSE in GDPS-SN with respect to the GDPS-CTL, whereas downward-pointing blue triangles indicate the opposite. Only verification using forecasts at full resolution is shown.

It is also interesting to compare GDPS-SN to GC. For the sake of fair comparison, this will only be done at low resolution. Predictions from GDPS-SN are closer to the radiosonde observations than GC in the upper and mid-level layers, except for dewpoint depression. Conversely, for the low-level layer, GC is closer to the observations, except for geopotential height (Fig. 12). The degradations with respect to dewpoint depression, also observed in the mid-level layer where spectral nudging is active, suggest that further gains could likely be achieved by nudging the humidity field in GEM towards GC. The results also suggest that extending spectral nudging to the boundary layer could be beneficial. This, however, would necessitate an AI model with more vertical levels in the boundary layer and fine-tuned to emulate the GDPS analyses rather than ECMWF-ERA5, for improved consistency with the GEM model's lower-boundary forcings.

The small but statistically significant GDPS-SN improvements over GC in the mid-level layer for temperature and zonal winds, two variables that are nudged toward GC, that grow with the integration time, are somewhat surprising (Fig. 12). This could be due to a positive feedback mechanism between the large and small scales in GEM. The averaging effect caused by the blend-

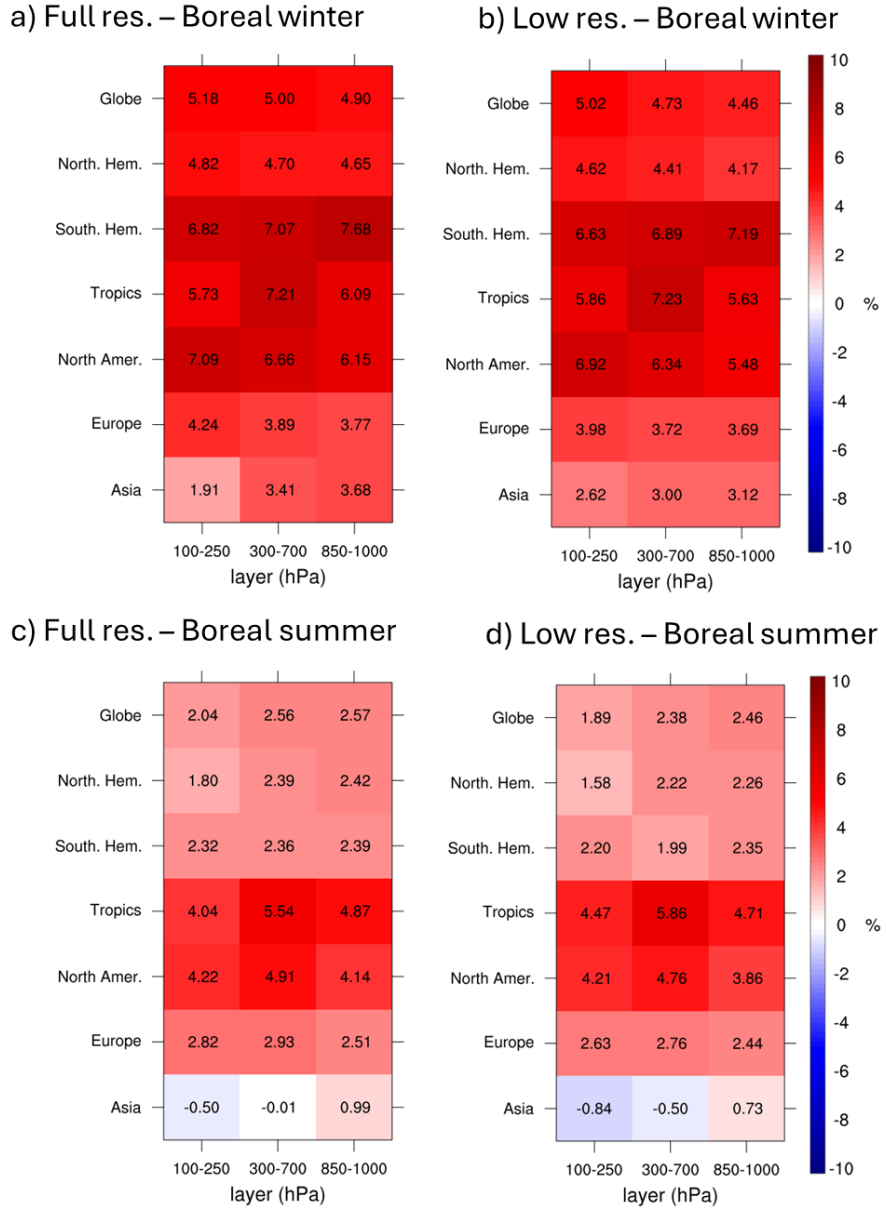


FIG. 11. Same as in Fig. 5, except that red shadings indicate a reduction of the RMSE in GDPS-SN with respect to GDPS-CTL, while blue shadings indicate the opposite.

ing of two forecasts due to a long relaxation time, as previously discussed in Section 5, may also be partly responsible for these improvements. Answering this question is, however, deemed outside the scope of this paper.

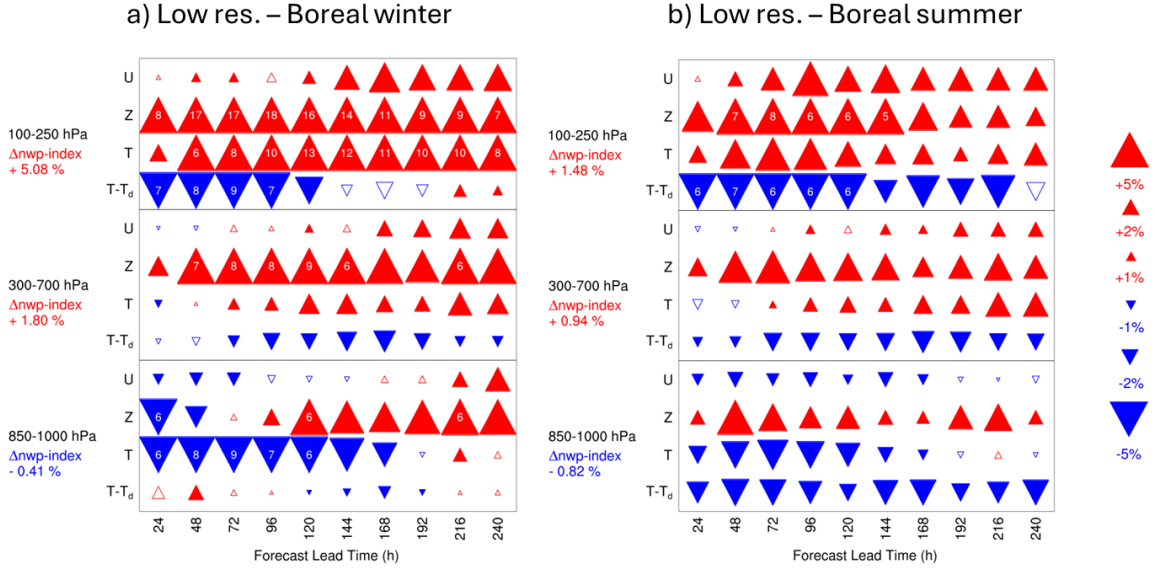


FIG. 12. Same as in Fig. 4, except that upward-pointing red triangles indicate a reduction of the RMSE in GDPS-SN with respect to GC, whereas downward-pointing blue triangles indicate the opposite. Only verification using forecasts at low resolution is shown but for both seasons.

Finally, the overall region-wise comparison of GDPS-SN and GC forecasts at low resolution (Fig. 13) shows that the results that were observed over the globe hold also relatively well for each of the subdomains. The fact that spectral nudging is applied only in the mid-level layer targeting only the synoptic scales, it considerably limits the ability of GDPS-SN to fully leverage the strengths of GC for seasonal periods and over regions where mesoscale near-surface conditions play a major role in determining the weather. This may explain the degradations seen over the tropics.

### c. Verification against ECMWF analyses

The comparison of GDPS-SN and GDPS-CTL forecasts against ECMWF-HRES analyses leads to very much similar results as the comparison against radiosonde observations, with general improvements for all variables, lead times and pressure levels (not shown). Figure 14 provides an example of improvements in anomaly correlation coefficient (ACC). For 500-hPa geopotential heights, the ACC improvements over the Northern Hemisphere region at forecast day 7 are equiv-

a) Low res. – Boreal winter      b) Low res. – Boreal summer

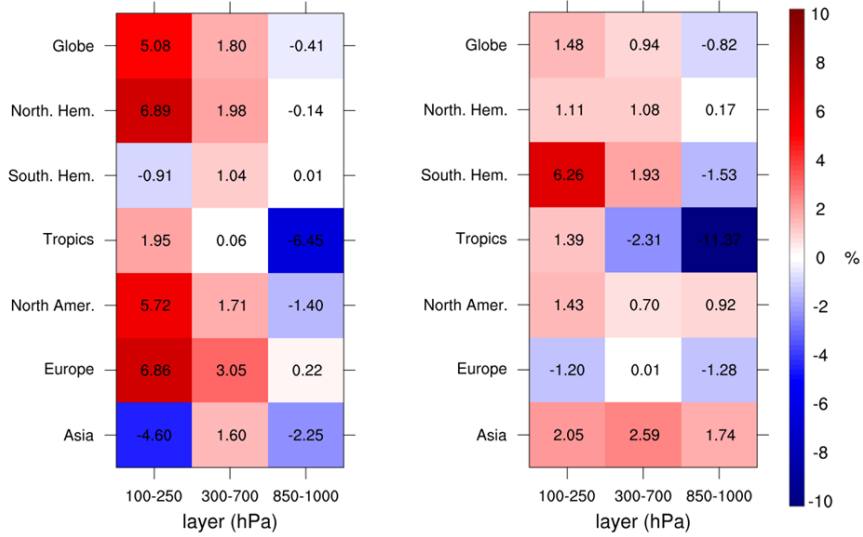


FIG. 13. Same as in Fig. 5, except that red shadings indicate a reduction of the RMSE in GDPS-SN with respect to GC, whereas blue shadings indicate the opposite. Only verification using forecasts at low resolution is shown.

alent to an 18-h increase in predictability during boreal winter and to an 8-h increase in summer. The corresponding ACC improvements over the Southern Hemisphere region are about 2 hours during austral winter and even exceed 24 hours during austral summer. There are also notable improvements in zonal wind ACC in the tropics that are equivalent to 24 hours or more (e.g., see Fig. 14b,e). The strength of GC in improving the ACC around day 5 (and beyond) is thus well leveraged by the hybrid system.

#### *d. Verification against surface observations*

For verification at the surface level, combined SYNOP, METAR and Surface Weather and marine OBservations (SWOB; available only over Canada and distributed by ECCC) data were used for surface pressure, screen-level temperature, dewpoint depression and anemometer-level wind speed. For precipitation, 24-h accumulation ground observations are subject to collection and quality control by the CAnadian Precipitation Analysis system (CaPA; Lespinas et al. (2015)).

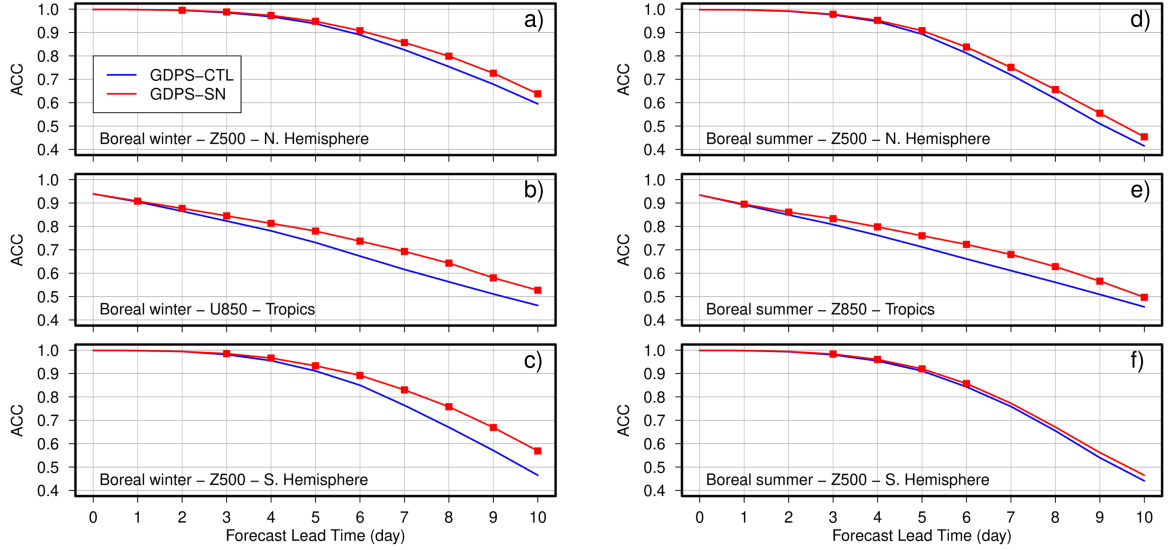
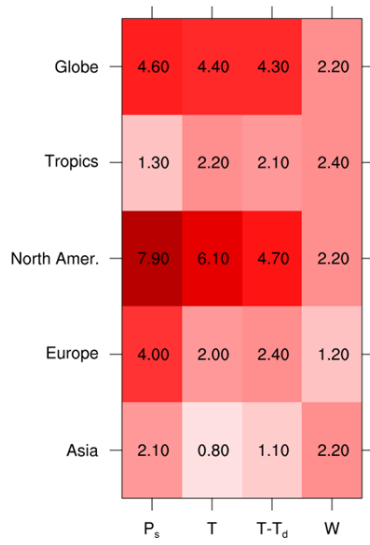


FIG. 14. Anomaly correlation coefficient against the ECMWF-HRES analyses with GDPS-CTL (blue) and GDPS-SN (red) for (a,d) northern hemisphere 500-hPa geopotential height, (b,e) tropical 850-hPa zonal wind, and (c,f) southern hemisphere 500-hPa geopotential height. Results are presented for 60 cases of boreal winter 2022 (left column: a–c) and 62 cases of boreal summer 2022 (right column: d–f). No marker at a pressure level implies that the null hypothesis, stating that the statistics of the two samples are the same, cannot be rejected based on the 95th percentile.

Any data pertaining to stations with an altitude difference larger than 100 m with respect to GDPS orography, along with any observed wind speed below  $1.5 \text{ m s}^{-1}$ , are excluded.

Comparison of GDPS-SN and GDPS-CTL using the forecast quality index (Eq. 3) is summarized in Fig. 15. Guidance by GDPS-SN is generally improved for all variables and regions. The improvements are, however, notably smaller than in the upper air, which is particularly the case for the tropics, where achieving considerable improvements appears to be difficult without introducing spectral nudging in the boundary layer. The same could be concluded for the screen-level thermodynamic variables and wind. On the other hand, the spectral nudging in the mid-level layer has the largest positive impact on the surface pressure via redistribution of upper-air mass. The improvements in boreal summer are notably smaller than in boreal winter, consistent with the upper-air verification.

a) Boreal winter



b) Boreal summer

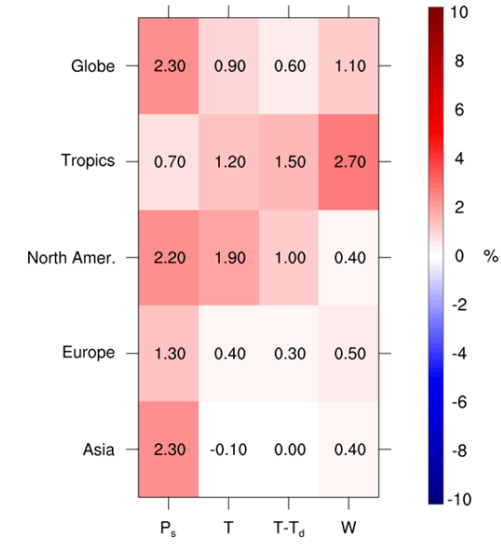


FIG. 15. Heatmap of the changes in the forecast quality index (Eq. 3) against combined SYNOP, SWOB and METAR observations for surface pressure ( $P_s$ ), screen-level temperature ( $T$ ), dewpoint depression ( $T - T_d$ ) and anemometer-level wind speed ( $W$ ) in various geographical domains for (a) 60 cases of boreal winter 2022 and (b) 62 cases of boreal summer 2022. Red shadings indicate a reduction of the RMSE in GDPS-SN with respect to GDPS-CTL, while blue shadings indicate the opposite.

The ability of the GPDS-SN to represent high-impact weather, such as high wind speeds and extreme temperatures, is not significantly different from the GDPS-CTL but, at the same time, it is substantially better than GC, which provides a strong example of the value added by the hybrid system over GC (Fig. 16). For example, the distribution of late-afternoon wind speeds over North America provided by GC shows a considerable shift toward lower values, which increases at high percentiles of the distribution, resulting in a  $-4 \text{ m s}^{-1}$  bias at the 99.9th percentile (Figs. 16 a, b). GDPS-CTL also has a negative bias but affecting only higher percentiles and, more importantly, GDPS-SN closely follows GDPS-CTL, with little or no sign of deceleration at extreme wind speeds for both seasons. GraphCast also suffers a 2-4 K cold bias at mid-to-high temperature percentiles over North America in summer, which has no impact on the GDPS-SN; its distribution aligns very well with the observations. GraphCast's poor performance with respect to the extremes can be partly explained by its lack of well-resolved fine scales that are generally critical for rep-

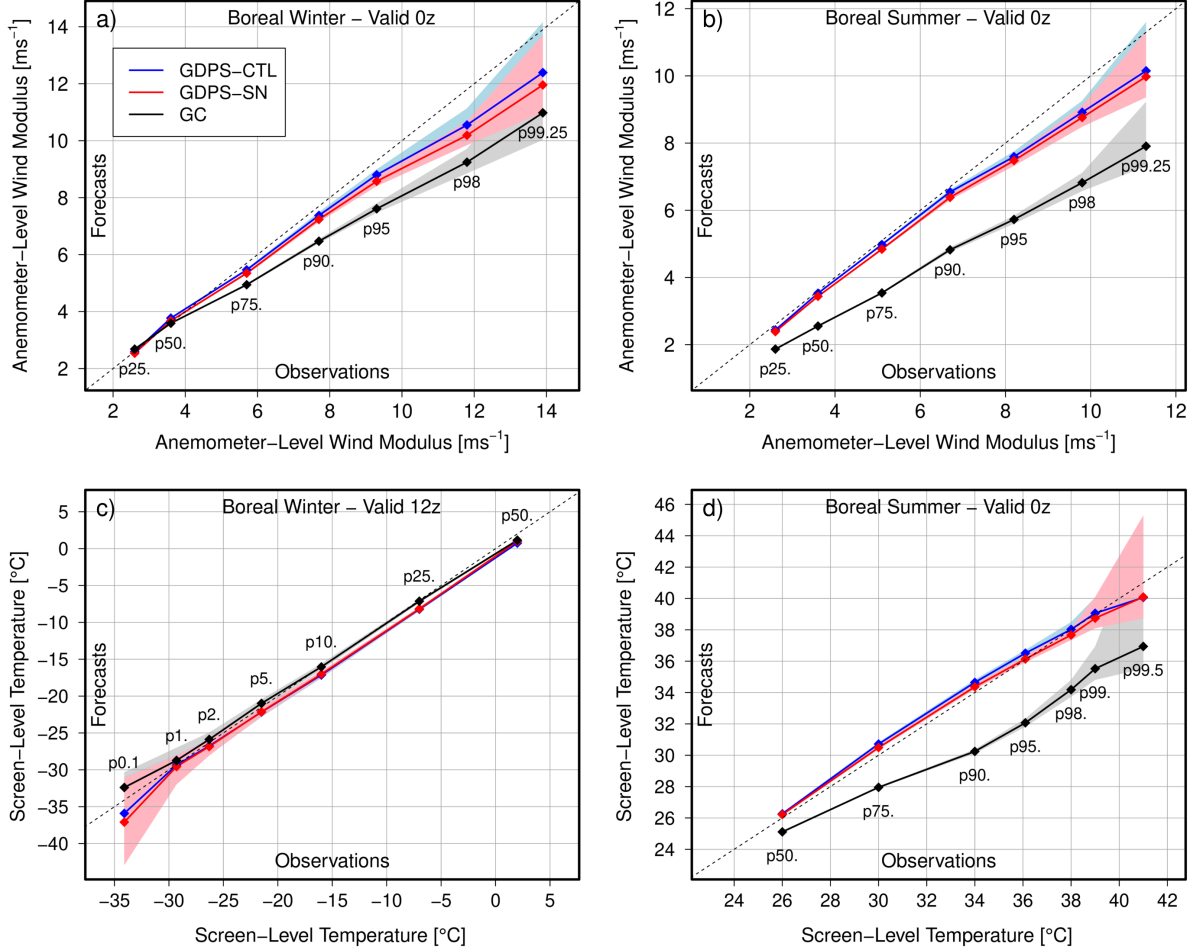


FIG. 16. Q-Q plots of day-5 GC (black), GDPS-CTL (blue) and GDPS-SN (red) forecasts against combined SYNOP, SWOB and METAR for: (a, b) anemometer-level wind speeds and (c, d) screen-level temperatures over North America for (a, c) 30 cases of boreal winter valid at (a) 00 and (c) 12 UTC, and (b, d) 31 cases of boreal summer valid 00 UTC. Local standard time over North America is mostly between UTC-5 and UTC-8 h. Diamond symbols denote selected percentiles with their values printed. Shadings denote 95% confidence bands for the inverse cumulative distribution functions, based on the Kolmogorov-Smirnov statistic.

resenting the extremes. Furthermore, inconsistencies in the surface forcing between ERA5 and GDPS analyses may also be a contributing factor for the observed underestimation of temperature extremes by GC. As the spectral nudging configuration presented in this study only targets synoptic scales and the boundary layer is allowed to evolve freely, GDPS-SN is not adversely affected by GC's limitations regarding the extremes.

Spectral nudging also significantly improves boreal winter precipitation forecast guidance over North America for a large range of thresholds from 1 to 50 mm day<sup>-1</sup>, mostly by reducing the false alarm ratio, with no reduction of probability of detection, which results in a reduced moist frequency bias and an improved equitable threat score (Fig. 17). These improvements seem to be mostly generated via an improved prediction of synoptic-scale flow. There is, however, not much of an impact of spectral nudging on summer precipitation over North America. Improving precipitation in summer, when weak synoptic forcings are prevalent, may necessitate the application of spectral nudging in the boundary layer.

#### *e. Tropical cyclone evaluation*

Evaluation of the impact of spectral nudging on the tropical cyclone (TC) forecast guidance is performed using the data from the International Best Track Archive for Climate Stewardship (IBTrACS; Knapp et al. 2010). For the results presented in this section, GDPS TC forecasts are matched with observations, by excluding from consideration any storm that is not detected by both GDPS and IBTrACS systems.

Spectral nudging improves TC trajectories by reducing the errors resulting from GDPS-CTL's tendency of predicting storms that move too slowly and veer too much to the right (with respect to its observed track), especially at lead times beyond day 5 (Figs. 18a and b). Conversely, there is little or no significant impact of spectral nudging on the TC intensity, as measured by the minimum central pressure and maximum sustained wind speed (Figs. 18c and d). Both GDPS-CTL and GDPS-SN have a similar weak intensity bias, which is a well-known weakness of the GEM model (see McTaggart-Cowan et al. (2024), for more details). Severe TC weak-intensity biases are typical of state-of-the-art deterministic AI-based forecast models (e.g., Bouallègue et al. (2024)) due to the smoothing effect caused by learning to minimize the MSE. However, AI-based models, including GC, are generally capable of predicting the TC trajectories with enhanced accuracy (Lam et al. 2022). Therefore, the improvements in the predicted trajectories by GDPS-SN show that the proposed hybrid system is capable of leveraging the well-documented strength of the AI-based models, without sacrificing TC intensity. Furthermore, these results suggest that the weak-intensity bias for TCs could be reduced in future by focusing on improving the physics-based NWP component of the hybrid system.

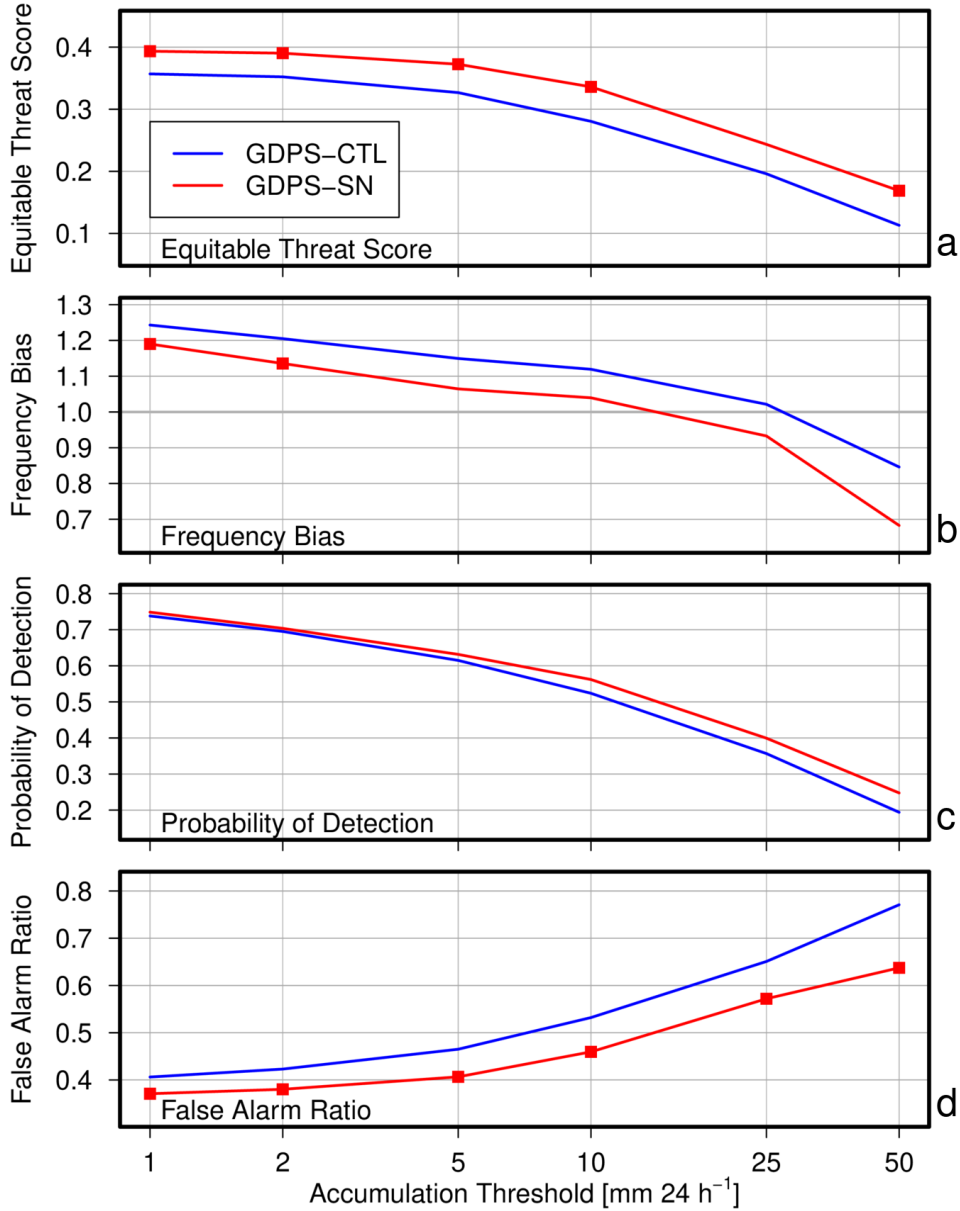


FIG. 17. Quantitative precipitation forecast verification for day 5 assessed by 24-hr precipitation threshold (accumulations between 108 and 132 h of integration) with the (a) equitable threat score, (b) frequency bias, (c) probability of detection, and (d) false alarm ratio. Results from the 60 GDPS-CTL (blue) and GDPS-SN (red) cases of boreal winter are compared to ground observations over North America used by CaPA. Red and blue line markers denote statistically significant differences in favor of GDPS-SN and GDPS-CTL, respectively. Significance is computed by bootstrapping 3-day data blocks consisting of forecast-observation pairs from all stations of a given region. No marker at a threshold level implies that the null hypothesis, stating that the statistics of the two samples are the same, cannot be rejected based on the 90th percentile.

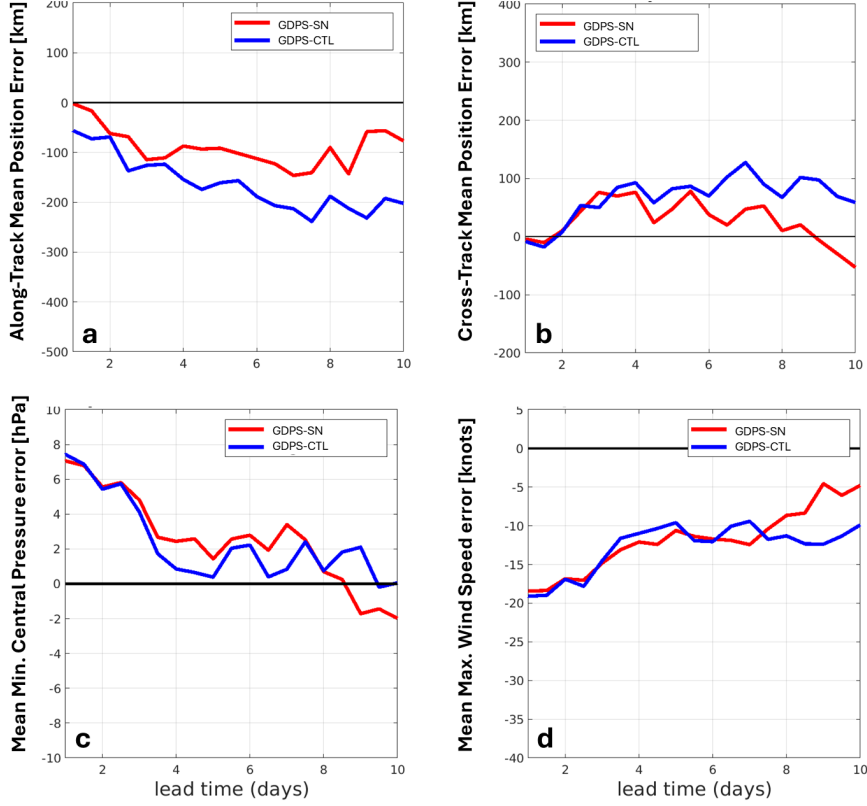


FIG. 18. Tropical cyclone tracking performance comparison of the GDPS-CTL (blue) and GDPS-SN (red) against IBTrACS data in three northern hemisphere basins (West Atlantic, East and West Pacific) for 62 cases of boreal summer 2022: (a) along-track and (b) cross-track mean position errors, (c) mean central pressure error and (d) mean maximum wind speed error. Negative along-track errors imply cyclones move too slowly and positive cross-track errors imply cyclones veer to much to the right with respect to the observed trajectory.

#### *f. Computational cost of spectral nudging*

The current implementation of spectral nudging in GEM with the presented optimal configuration leads to an increase of computational cost by approximately 25%. Due to the proof-of-concept nature of this study, no optimization of the informatics code has been performed. Therefore, the cost could be considerably reduced through future code optimization, especially for the spectral filter. Further improvements could be attained by considering time-varying nudging increments, where nudging would only be applied at time-steps close to the inference times of GC. These considerations however lie beyond the scope of this study.

## 7. Summary and Future Work

The recent emergence of AI models has begun to disrupt the operational weather forecasting paradigm which has long been dominated by the physics-based NWP models. Naturally, serious questions about the future role of AI and NWP models in operational forecasting are arising. For instance, are AI models capable of adding any reliable and meaningful value for weather services, or will NWP models eventually disappear from the forecasting landscape and be replaced by AI models? This study attempts to address these pressing questions by choosing the GEM and GC models to represent the two forecasting approaches.

First, by comparing and contrasting the GEM and GC models, their relative strengths and weaknesses are identified. Skill verification against observations and GDPS analyses reveals that GC suffers from excessive fine-scale smoothing, affecting scales as large as 2500 km beyond day 3 of a 10-day forecast. However, despite smoothing, the results demonstrate that large-scale features (wavelength $>2500$  km) in GC exhibit better skill compared to GEM, which is evidenced by increased spectral coherence relative to the GDPS analyses and reduced STDE against radiosonde observations.

Inspired by the improved large-scale skill of GC, a hybrid NWP-AI system – namely, GDPS-SN – has been developed to produce global forecasts where GEM-predicted large scales in horizontal wind and temperature are spectrally nudged toward inferences from GC. This hybrid system is capable of generating real-time forecasts with accuracy that surpasses ECCC's operational GPDS. For example, RMSE of the 500-hPa geopotential height is reduced by 5-10%, with an overall predictability improvement of 12-18 hours, peaking at day 7 of a 10-day forecast. Notably, trajectories of tropical cyclones are predicted with enhanced accuracy without significant changes in intensity. Regarding precipitation, statistically significant improvements are obtained in equitable threat score, frequency bias and false alarm ratio, particularly in non-summer regimes. Skill enhancements with GDPS-SN are generally found to be more remarkable in winter when large scales apparently play a more critical role in determining weather at the regional level.

In addition to enhancing the skill and predictability of GEM, the proposed hybrid NWP-AI system is shown to generate the full spectra of fine scales that is missing in GC inferences. Furthermore, the new system is capable of producing all the usual forecast variables that operational meteorologists rely on for forecasting weather in general and high-impact events in particular.

Comparisons against near-surface observations have revealed that – unlike GC, which has a limited ability to capture the extremes in wind speed and temperature – weather extremes predicted by GDPS-SN closely follow the operational GDPS-CTL. This implies that the fine scales predicted by GPDS-SN not only possess similar level of energy as GDPS-CTL, they are also comparable in terms of skill.

Other aspects of near-surface predictions from GDPS-SN, however, show relatively modest improvement (e.g., screen-level scores). Lack of vertical resolution in the boundary layer in GC-13 and inconsistencies in surface forcing (such as orography) between ERA5 and GDPS analyses were the reasons why nudging in the boundary layer has not been considered in this study. This largely explains the less-than-remarkable near-surface performance of GDPS-SN. However, work is currently in progress at ECCC to fine-tune GC to emulate the operational GDPS analyses. This fine-tuned version is expected to enhance GC’s skill with the 37-level version, particularly in the stratosphere and the boundary layer. Any such improvement could be easily leveraged by the hybrid system in the near future. Importantly, a fine-tuned GC would allow for nudging in the boundary layer which is expected to result in further enhancement of near-surface skill with GDPS-SN.

Finally, results from the proposed hybrid NWP-AI system imply that, rather than viewing AI and NWP models as two competing paradigms, it is likely more prudent to consider these forecasting methods as complementary. A well-designed fusion of these two approaches can significantly mitigate their individual limitations while allowing for harnessing their respective strengths to provide better meteorological guidance. Therefore, instead of focusing on efforts to replace one with the other, future research should prioritize improving both NWP and AI models.

*Acknowledgments.* The authors would like to thank their retired colleague, Dr. Bertrand Denis, for being one of the individuals who early on highlighted the potential benefits of large-scale spectral nudging in leveraging AI-based models.

## APPENDIX A

### The spherical harmonics-based global filter

Isolation of the large scales in the predictions from GDPS and GC is required to compare the skill possessed at those scales. It is achieved through the application of a spectral filter. The physical outputs from the models at a given pressure level are first transformed to the spectral space through spherical harmonic-based decomposition. This is followed by the application of the filter,  $f_n$ , as proposed by Sardeshmukh and Hoskins (1984). The functional form of the filter is given by

$$f_n = \exp \left[ - \left( \frac{n(n+1)}{n_o(n_o+1)} \right)^r \right], \quad (\text{A1})$$

where  $n$  denotes the total wavenumber,  $n_o$  is the cut-off total wavenumber and the exponent  $r$  is a non-dimensional parameter related to the sharpness of the filter response. Based on the spectral comparison of the GDPS and GC predictions, the filter is configured by setting  $n_0 = 30$  and  $r = 4$ . As shown in Fig. A1, the resulting filtered fields fully retain amplitudes for scales associated with approximately  $n < 20$  (wavelength > 2000 km) and fully removes scales corresponding to  $n > 40$  (wavelength < 1000 km). The physical fields reconstructed from the filtered spectra leads to the desired filtered fields.

## APPENDIX B

### The DCT-based filter for spectral nudging

Two-dimensional DCT and its implementation in GEM for spectral nudging in limited-area modelling are well documented in the existing literature (Denis et al. 2002; Husain et al. 2014). For global simulations based on the Yin-Yang grid system, nudging is applied to the LAM sub-domains associated with the Yin and Yang grids separately. The first step in spectral nudging is to compute the coefficients,  $\hat{f}(m, n)$ , of DCT of  $(F_{GC} - F_{GEM})$ , which determines the nudging increment (see

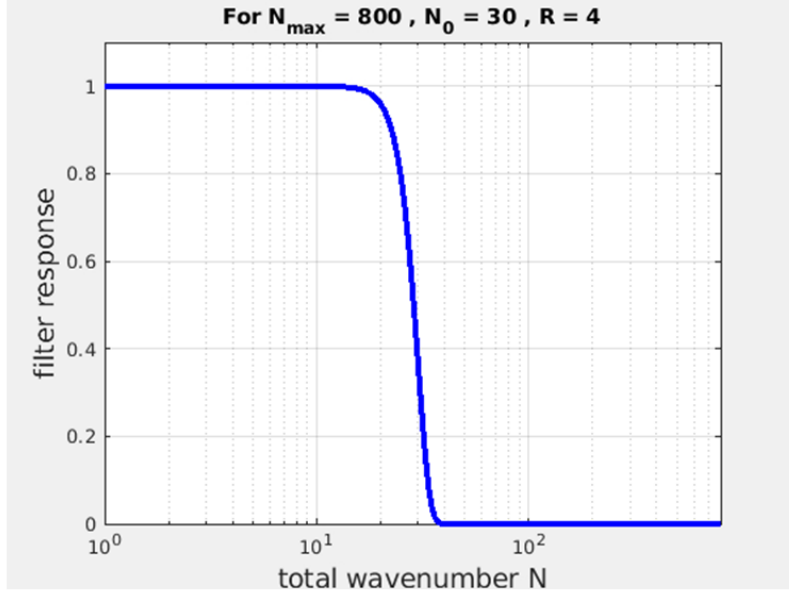


FIG. A1. Response of the spherical-harmonics based spectral filter with  $n_0 = 30$  and  $r = 4$  (see Eq. A1).

Eq. 4). For each of the Yin-Yang sub-domains,  $m$  and  $n$  denote the one-dimensional horizontal wavenumbers. In the second step,  $\hat{f}(m, n)$  is subjected to a spectral filter,  $f_F(m, n)$ , of the form

$$f_F(m, n) = \begin{cases} 0.0, & \text{if } \hat{\alpha} > \lambda_{LS}/\lambda_{SS} \\ \left[ \cos \left( \frac{\pi}{2} \frac{\alpha \lambda_{LS}/(2\Delta) - 1}{\lambda_{LS}/\lambda_{SS} - 1} \right) \right]^2, & \text{if } 1.0 < \hat{\alpha} \leq \lambda_{LS}/\lambda_{SS} \\ 1.0, & \text{if } \hat{\alpha} \leq 1.0 \end{cases} \quad (\text{B1})$$

where  $\Delta$  denotes the model grid spacing,  $\alpha$  is the normalized two-dimensional wavenumber given by  $\alpha = \sqrt{\frac{m^2}{N_i^2} + \frac{n^2}{N_j^2}}$  associated with each of the Yin-Yang sub-domains of size  $(N_i \times N_j)$ , and  $\hat{\alpha} = \alpha \lambda_{LS}/(2\Delta)$ .

Figures B1a and B1b illustrate the response of this DCT-based filter for a configuration based on  $\lambda_{LS} = 1500$  km and  $\lambda_{SS} = 1000$  km. The figures demonstrate that the DCT-based filter is capable of targeting the desired scales for the individual Yin-Yang sub-domains. The response of the filter over the globe was determined by inspecting the spectral variance ratio of the filtered and unfiltered fields over a global Gaussian grid with respect to a spherical harmonics-based decomposition.

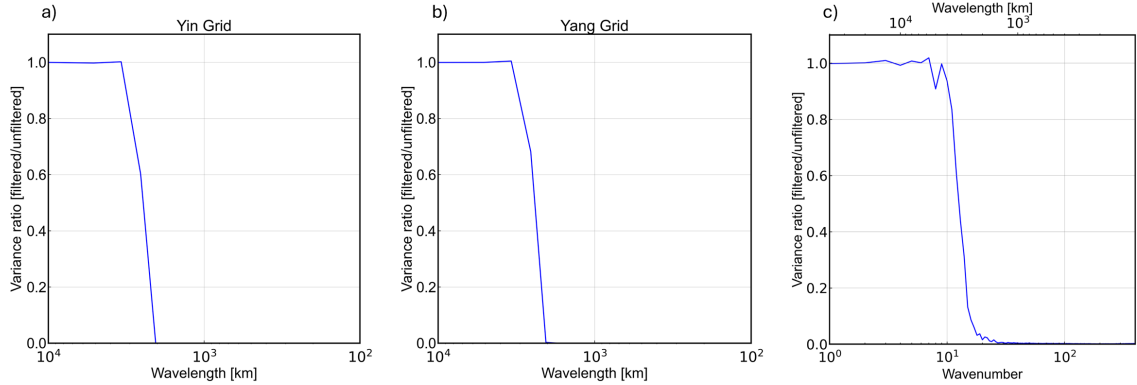


FIG. B1. Response of the DCT-based filter (see Eq. B1) with respect to the (a) Yin grid, (b) Yang grid, and (c) a global Gaussian grid.

The corresponding results are presented in Fig. B1c. The figure reveals that, even though DCT is primarily designed for LAMs where curvature effects of spherical surfaces are neglected, its application on global Yin-Yang grid does not result in any major issue as the filter is found to result in an acceptable response.

## References

Bi, K., L. Xie, H. Zhang, X. Chen, X. Gu, and Q. Tian, 2022: Pangu-weather: A 3d high-resolution model for fast and accurate global weather forecast. *arXiv preprint*, <https://doi.org/https://doi.org/10.48550/arXiv.2211.02556>.

Bi, K., L. Xie, H. Zhang, X. Chen, X. Gu, and Q. Tian, 2023: Accurate medium-range global weather forecasting with 3d neural networks. *Nature*, **619**, 533–538.

Bouallègue, Z. B., and Coauthors, 2024: The rise of data-driven weather forecasting: a first statistical assessment of machine learning-based weather forecasts in an operational-like context. *Bull. Amer. Meteor. Soc.*, **105**, E864–E883.

Busuioc, A., R. Tomozeiu, and C. Cacciamani, 2008: Statistical downscaling model based on canonical correlation analysis for winter extreme precipitation events in the emilia romagna region. *Int. J. Climatol.*, **28**, 449–464.

Caron, J.-F., and M. Buehner, 2022: Implementation of scale-dependent background-error covariance localization in the Canadian Global Deterministic Prediction System. *Wea. Forecast.*, **37**, 1567–1580.

Casati, B., and Coauthors, 2008: Forecast verification: Current status and future directions. *Meteorol. App.*, **15**, 3–18.

Charney, J., 1971: Geostrophic turbulence. *J. Atmos. Sci.*, **28**, 1087–1095.

Chen, K., and Coauthors, 2023a: FengWu: Pushing the skillful global medium-range weather forecast beyond 10 days lead. *arXiv preprint*, <https://doi.org/https://doi.org/10.48550/arXiv.2304.02948>.

Chen, L., X. Zhong, F. Zhang, Y. Cheng, Y. Xu, Y. Qi, and H. Li, 2023b: FuXi: a cascade machine learning forecasting system for 15-day global weather forecast. *npj Clim. Atmos. Sci.*, **6**, <https://doi.org/https://doi.org/10.1038/s41612-023-00512-1>.

Cheng, C., C. Fu, and Z. Huang, 2014: Possible impacts of climate change on wind gusts under downscaled future climate conditions: Updaed for canada. *J. Clim.*, **27**, 1255–1270.

Denis, B., J. Côté, and R. Laprise, 2002: Spectral decomposition of two-dimensional atmospheric fields on limited-area domains using the discrete cosine transform (DCT). *Mon. Wea. Rev.*, **130**, 1812–1829.

ECCC, 2024: Global Deterministic Prediction System (GDPS) – Update from version 8.1.0 to version 9.0.0. *Canadian Meteorological Centre Tech. Note*, URL [https://collaboration.cmc.ec.gc.ca/cmc/cmoi/product\\_guide/docs/lib/technote\\_gdps-900\\_e.pdf](https://collaboration.cmc.ec.gc.ca/cmc/cmoi/product_guide/docs/lib/technote_gdps-900_e.pdf).

Girard, C., and Coauthors, 2014: Staggered vertical discretization of the Canadian Environmental Multiscale (GEM) model using a coordinate of the log-hydrostatic-pressure type. *Mon. Wea. Rev.*, **120**, 113–123.

Hersbach, H., and Coauthors, 2020: The ERA5 global reanalysis. *Q. J. R. Meteorol. Soc.*, **146**, 1999–2049.

Husain, S., C. Girard, L. Separovic, A. Plante, and S. Corvec, 2021: On the progressive attenuation of finescale orography contributions to the vertical coordinate surfaces within a terrain-following coordinate system. *Mon. Wea. Rev.*, **148**, 4143–4158.

Husain, S., L. Separovic, W. Yu, and D. Fernig, 2014: Extended-range high-resolution dynamical downscaling over a continental-scale spatial domain with atmospheric and surface nudging. *J. Geophys. Res.: Atmos.*, **119**, 13 720–13 750.

Husain, S. Z., and C. Girard, 2017: Impact of consistent semi-Lagrangian trajectory calculations on numerical weather prediction performance. *Mon. Wea. Rev.*, **145**, 4127–4150.

Husain, S. Z., C. Girard, A. Qaddouri, and A. Plante, 2019: A new dynamical core of the Global Environmental Multiscale (GEM) model with a height-based terrain-following vertical coordinate. *Mon. Wea. Rev.*, **147**, 2555–2578.

Keisler, R., 2022: Forecasting global weather with graph neural networks. *arXiv preprint*, <https://doi.org/https://doi.org/10.48550/arXiv.2202.07575>.

Knapp, K., M. Kruk, D. Levinson, H. Diamond, and C. Neumann, 2010: The International Best Track Archive for Climate Stewardship (IBTrACS). *Bull. Amer. Meteor. Soc.*, **91**, 363–376.

Lam, R., and Coauthors, 2022: Graphcast: Learning skillful medium-range global weather forecasting. *arXiv preprint*, <https://doi.org/https://doi.org/10.48550/arXiv.2212.12794>.

Lam, R., and Coauthors, 2023: Learning skillful medium-range global weather forecasting. *Science*, **382**, 1416–1421.

Lang, S., M. Rodwell, and D. Schepers, 2023: IFS upgrade brings many improvements and unifies medium-range resolutions. *ECMWF Newsletter*, **176**, 21–28.

Leduc, M., and R. Laprise, 2009: Regional climate model sensitivity to domain size. *Clim. Dyn.*, **32**, 833–854.

Lespinas, F., V. Fortin, G. Roy, P. Rasmussen, and T. Stadnyk, 2015: Performance evaluation of the Canadian Precipitation Analysis (CaPA). *J. Hydrometeor.*, **16**, 2045–2064.

McTaggart-Cowan, R., and Coauthors, 2019: Modernization of atmospheric physics parameterization in Canadian NWP. *J. Adv. Model. Earth Syst.*, **11**, 3593–3635, <https://doi.org/https://doi.org/10.1029/2019MS001781>.

McTaggart-Cowan, R., and Coauthors, 2024: Reducing a tropical cyclone weak-intensity bias in a global numerical weather prediction system. *Mon. Wea. Rev.*, **152**, 837–863.

Omrani, H., P. Drobinski, and T. Dubos, 2012: Spectral nudging in regional climate modelling: how strongly should we nudge. *Q. J. Roy. Met. Soc.*, **138**, 1808–1813.

Pathak, J., and Coauthors, 2022: FourCastNet: a global data-driven high-resolution weather model using adaptive fourier neural operators. *arXiv preprint*, <https://doi.org/https://doi.org/10.48550/arXiv.2202.11214>.

Price, I., and Coauthors, 2024: GenCast: Diffusion-based ensemble forecasting for medium-range weather. *arXiv preprint*, <https://doi.org/https://doi.org/10.48550/arXiv.2312.15796>.

Privé, N., R. Errico, R. Todling, and A. Akkraoui, 2021: Evaluation of adjoint-based observation impacts as a function of forecast length using an observing system simulation experiment. *Q. J. R. Meteorol. Soc.*, **147**, 121–138.

Qaddouri, A., and V. Lee, 2011: The Canadian Global Environmental Multiscale model on the Yin-Yang grid system. *Q. J. R. Meteorol. Soc.*, **137**, 1913–1926.

Sardeshmukh, P., and B. Hoskins, 1984: Spatial smoothing on the sphere. *Mon. Wea. Rev.*, **112**, 2524–2529.

Schubert-Frisius, M., F. Feser, H. von Sotrch, and S. Rast, 2017: Optimal spectral nudging for global dynamic downscaling. *Mon. Wea. Rev.*, **145**, 909–927.

Skamarock, W., 2004: Evaluating mesoscale NWP models using kinetic energy spectra. *Mon. Wea. Rev.*, **132**, 3019–3032.

Skamarock, W., S. Park, J. Klemp, and C. Snyder, 2014: Atmospheric Kinetic Energy Spectra from Global High-Resolution Nonhydrostatic Simulations. *J. Atmos. Sci.*, **71**, 4369–4381.

Smith, G., and Coauthors, 2018: Impact of coupling with an ice-ocean model on global medium range NWP forecast skill. *Mon. Wea. Rev.*, **146**, 1157–1180.

von Storch, H., H. Langenberg, and F. Feser, 2000: A spectral nudging technique for dynamical downscaling purposes. *Mon. Wea. Rev.*, **128**, 3664–3673.

Waldron, K., J. Paegle, and J. Horel, 1996: Sensitivity of a spectrally filtered and nudged limited-area model to outer model options. *Mon. Wea. Rev.*, **124**, 529–547.

Yu, W., R. Benoit, C. Girard, A. Glazer, D. Lemarquis, J. Salmon, and J.-P. Pinard, 2006: Wind Energy Simulation Toolkit (WEST): A Canadian wind mapping and forecasting system for wind energy industry . *Wind Eng.*, **30**, 15–33.